

1 **Constraint of non-methane volatile organic compound emissions with**  
2 **TROPOMI HCHO observations and its impact on summertime**  
3 **surface ozone simulation over China**

4  
5 Shuzhuang Feng<sup>1</sup>, Fei Jiang<sup>1,2,5\*</sup>, Tianlu Qian<sup>3</sup>, Nan Wang<sup>4</sup>, Mengwei Jia<sup>1</sup>, Songci  
6 Zheng<sup>1</sup>, Jiansong Chen<sup>6</sup>, Fang Ying<sup>6</sup>, Weimin Ju<sup>1,2</sup>

7  
8 <sup>1</sup> *Jiangsu Provincial Key Laboratory of Geographic Information Science and*  
9 *Technology, International Institute for Earth System Science, Nanjing University,*  
10 *Nanjing, 210023, China*

11 <sup>2</sup> *Jiangsu Center for Collaborative Innovation in Geographical Information Resource*  
12 *Development and Application, Nanjing, 210023, China*

13 <sup>3</sup> *School of Geographic and Biologic Information, Nanjing University of Posts and*  
14 *Telecommunications, Nanjing, 210023, China*

15 <sup>4</sup> *College of Carbon Neutrality Future Technology, Sichuan University, Chengdu,*  
16 *610207, China*

17 <sup>5</sup> *Frontiers Science Center for Critical Earth Material Cycling, Nanjing University,*  
18 *Nanjing, 210023, China*

19 <sup>6</sup> *Hangzhou Municipal Ecology and Environment Bureau, Hangzhou, 310020, China*

20  
21  
22  
23  
24  
25  
26  

---

\* Corresponding author: Tel.: +86-25-83597077; Fax: +86-25-83592288; E-mail address: jiangf@nju.edu.cn

27 **Abstract**

28 Non-methane volatile organic compounds (NMVOC), serving as crucial precursors  
29 of O<sub>3</sub>, have a significant impact on atmospheric oxidative capacity and O<sub>3</sub> formation.  
30 However, both anthropogenic and biogenic NMVOC emissions remain subject to  
31 considerable uncertainty. Here, we extended the Regional multi-Air Pollutant  
32 Assimilation System (RAPAS) with the EnKF algorithm to optimize NMVOC  
33 emissions in China by assimilating TROPOMI HCHO retrievals. We also  
34 simultaneously optimize NO<sub>x</sub> emissions by assimilating in-situ NO<sub>2</sub> observations to  
35 address the chemical feedback among VOC-NO<sub>x</sub>-O<sub>3</sub>. Furthermore, a process-based  
36 analysis was employed to quantify the impact of NMVOC emission changes on  
37 various chemical reactions related to O<sub>3</sub> formation and depletion. NMVOC  
38 emissions exhibited a substantial reduction of 50.2%, especially in forest-rich areas  
39 of central and southern China, revealing a prior overestimation of biogenic NMVOC  
40 emissions. Compared with the forecast with prior NMVOC emissions, the forecast  
41 with posterior emissions ~~The RAPAS~~ significantly improved HCHO simulations,  
42 reducing biases by 75.7%, indicating a notable decrease in posterior emission  
43 uncertainties. ~~Moreover, the forecast with posterior NMVOC emissions also~~  
44 effectively significantly corrected the overestimation of O<sub>3</sub> in forecast with prior  
45 emissions overestimation in O<sub>3</sub> simulations, reducing biases by 49.3%. This can be  
46 primarily attributed to a significant decrease in the RO<sub>2</sub> + NO reaction rate and an  
47 increase in the NO<sub>2</sub> + OH reaction rate in the afternoon, thus limiting O<sub>3</sub> generation.  
48 Sensitivity analyses emphasized the necessity of considering both NMVOC and NO<sub>x</sub>  
49 emissions for a comprehensive assessment of O<sub>3</sub> chemistry. This study enhances our  
50 understanding of the effects of NMVOC emissions on O<sub>3</sub> production and can  
51 contribute to the development of effective emission reduction policies.

52

53

54

55 **Keywords**

56 NMVOC emissions, O<sub>3</sub> pollution, Emission inversion, HCHO column retrievals, Data  
57 assimilation

58

## 59 **1 Introduction**

60 Since the Chinese government implemented the Air Pollution Prevention and Control  
61 Action Plan in 2013, there has been a notable reduction in NO<sub>x</sub> emissions (Zheng et al.,  
62 2018). However, despite these advancements, the issue of O<sub>3</sub> pollution persists and, in  
63 certain cases, has shown signs of worsening (Ren et al., 2022). The increase in O<sub>3</sub>  
64 concentration can be attributed not only to adverse meteorological conditions but also  
65 predominantly to unbalanced joint control of non-methane volatile organic compounds  
66 (NMVOCs) and nitrogen oxides (NO<sub>x</sub>) (Li et al., 2020). NMVOCs are vital precursors  
67 of O<sub>3</sub> and have a substantial impact on the atmospheric oxidation capacity, thereby  
68 altering the lifetimes of other pollutants. Accurately quantifying NMVOC emissions  
69 holds significant importance in investigating their impact on O<sub>3</sub> chemistry and in  
70 formulating emission reduction policies.

71 Anthropogenic NMVOC emissions have traditionally been estimated using a “bottom-  
72 up” method. However, the accuracy and timeliness of these estimations face challenges  
73 owing to the scarcity of local measurements for emission factors, the incompleteness  
74 and unreliability of activity data, and the diverse range of species and technologies  
75 involved (Cao et al., 2018; Hong et al., 2017). Furthermore, uncertainties arise in  
76 model-ready NMVOC emissions due to spatial and temporal allocations using various  
77 “proxy” data for different source sectors (Li et al., 2017a). Li et al. (2021) reported  
78 substantial discrepancies among emission estimates in various studies, ranging 23% to  
79 56%. Biogenic NMVOC emissions are typically estimated using models like the Model  
80 of Emissions of Gases and Aerosols from Nature (MEGAN) (Guenther et al., 2012) and  
81 the Biogenic Emission Inventory System (BEIS) (Pierce et al., 1998). NMVOC  
82 emissions result from the multiplication of plant-specific standard emission rates by  
83 dimensionless activity factors. Nonetheless, apart from inaccuracies in the distribution  
84 of plant functional types, empirical parameterization, especially concerning responses  
85 to temperature and drought stress, can introduce substantial uncertainties (Angot et al.,  
86 2020; Seco et al., 2022; Jiang et al., 2018). Warneke et al. (2010) determined isoprene  
87 emission rates through field measurements and conducted a comparison with MEGAN  
88 and BEIS estimates, revealing a notable tendency for MEGAN to overestimate  
89 emissions, while BEIS consistently underestimated them. Similarly, Marais et al. (2014)  
90 found that MEGAN's isoprene emission estimates were 5-10 times higher than the  
91 canopy-scale flux measurements obtained from African field campaigns.

92 A top-down approach, utilizing observed data, has been developed for estimating VOCs  
93 emissions. For instance, based on aircraft and ground-based field measurements, the  
94 source-receptor relationships algorithm with Lagrangian particle dispersion model  
95 (Fang et al., 2016), mixed layer gradient techniques (Mo et al., 2020), eddy covariance  
96 flux measurements (Yuan et al., 2015), and box model (Wang et al., 2020) have been  
97 employed to complement or verify bottom-up results. However, these approaches do  
98 not comprehensively consider the complex nonlinear chemical reactions and transport  
99 processes that VOCs undergo in the atmosphere. Formaldehyde (HCHO) and glyoxal  
100 (CHOCHO) in the atmosphere serve as crucial oxidization intermediates for various  
101 VOCs (Hong et al., 2021; Liu et al., 2012). Satellite-based observations can readily  
102 detect their presence in the form of vertical column density (VCD) from space, making  
103 them widely utilized for estimating NMVOC emissions. A commonly used approach  
104 assumes that the observed HCHO/CHOCHO columns are locally linearly correlated  
105 with VOC emission rates (Palmer et al., 2006; Liu et al., 2012). However, this approach  
106 does not consider the spatial offset resulting from chemistry reactions and transport  
107 processes. Chaliyakunnel et al. (2019) conducted a Bayesian analysis to derive an  
108 optimal estimate of VOC emissions using HCHO measurements over the Indian  
109 subcontinent. Their results indicated that biogenic VOC emissions modeled by  
110 MEGANv2.1 were overestimated by approximately 30–60%, whereas anthropogenic  
111 VOC emissions derived from the RETRO inventory were underestimated by 13–16%.  
112 Cao et al. (2018) employed the GEOS-Chem model and its adjoint, incorporating  
113 tropospheric HCHO and CHOCHO column data from the GOME-2A and OMI  
114 satellites as constraints, to quantify Chinese NMVOC emissions. They demonstrated a  
115 low bias in the MEGAN model, in contrast to the significant overestimation shown in  
116 Bauwens et al. (2016), especially in southern China.

117 Several investigations have been conducted to explore the implications of inverted  
118 VOC emissions on surface O<sub>3</sub>. For instance, using the Eulerian box model, Zhou et al.  
119 (2023) employed concurrent VOC measurements to constrain anthropogenic VOC  
120 emissions. This led to improved simulations of VOCs and O<sub>3</sub>, with a reduction in high  
121 emissions by 15%–36% in the Pearl River Delta (PRD) region. Local model biases in  
122 simulating the oxidation of NMVOCs and O<sub>3</sub> are closely related to uncertainties in NO<sub>x</sub>  
123 emissions (Wolfe et al., 2016; Chan Miller et al., 2017). To tackle these critical  
124 questions, Kaiser et al. (2018) applied an adjoint algorithm to estimate isoprene

125 emission over the southeast US by downwardly adjusting anthropogenic  $\text{NO}_x$  emissions  
126 by 50% to rectify  $\text{NO}_2$  simulations. Their findings indicated that isoprene emissions  
127 from MEGAN v2.1 were overestimated by an average of 40%, slightly lower than the  
128 50% reduction in Bauwens et al. (2016). Souri et al. (2020) simultaneously optimized  
129 NMVOC and  $\text{NO}_x$  emissions utilizing OMPS-NM HCHO and OMI  $\text{NO}_2$  retrievals in  
130 East Asia. They found that predominantly anthropogenic NMVOC emissions from  
131 MIX-Asia 2010 increased over the North China Plain (NCP), whereas predominantly  
132 biogenic NMVOC emissions from MEGAN v2.1 decreased over southern China after  
133 the adjustment. Unfortunately, the posterior simulations exacerbated the overestimation  
134 of  $\text{O}_3$  levels in northern China.

135 Most studies regarding the inversion of NMVOC emissions or its impact on  $\text{O}_3$   
136 neglected the uncertainties associated with  $\text{NO}_x$ -dependent production or loss of  
137 NMVOC oxidation and  $\text{O}_3$ . An iteratively nonlinear joint inversion of  $\text{NO}_x$  and  
138 NMVOCs using multi-species observations is expected to minimize the uncertainties  
139 in their emissions and is well-suited to address the intricate relationship among VOC-  
140  $\text{NO}_x$ - $\text{O}_3$ . In this study, we extended the Regional multi-Air Pollutant Assimilation  
141 System (RAPAS) upon the ensemble Kalman filter (EnKF) assimilation algorithm to  
142 enhance the optimization of NMVOC emissions over China, utilizing the  
143 TROPOspheric Monitoring Instrument (TROPOMI) HCHO retrievals with high spatial  
144 coverage and resolution. To more accurately quantify the impact of NMVOC emissions  
145 on  $\text{O}_3$ ,  $\text{NO}_x$  emissions were simultaneously adjusted using nationwide in-situ  $\text{NO}_2$   
146 observations. Process analysis was subsequently employed to quantify various  
147 chemical pathways associated with  $\text{O}_3$  formation and loss. Through a top-down  
148 constraint on both emissions, this study aims to offer a more scientific insight into the  
149 consequences of optimizing NMVOC emissions on  $\text{O}_3$  and contribute to the  
150 development of appropriate emission reduction policies.

## 151 **2 Data and Methods**

### 152 **2.1 Data Assimilation System**

153 The RAPAS system (Feng et al., 2023) has been developed based on a regional  
154 chemical transport model (CTM) and ensemble square root filter (EnSRF) assimilation  
155 modules (Whitaker and Hamill, 2002), which are employed for simulating atmospheric  
156 compositions and inferring anthropogenic emissions by assimilating surface

157 observations, respectively (Feng et al., 2022; Feng et al., 2020). The inversion process  
158 follows a two-step procedure within each inversion window, in which the emissions are  
159 inferred first and then input into the CMAQ model to simulate initial conditions of the  
160 next window. Meanwhile, the optimized emissions are transferred to the next window  
161 as prior emissions. –The two-step inversion strategy facilitates error propagation and  
162 iterative emission optimization, which have proven the superiority and robustness of  
163 our system in estimating emissions (Feng et al., 2023). In this study, we extended the  
164 data frame to include the assimilation of TROPOMI HCHO retrievals for optimizing  
165 NMVOC emissions. Concise descriptions of the forecast model, data assimilation  
166 approach, and experimental settings follow.

### 167 **2.1.1 Atmospheric Transport Model**

168 The Weather Research and Forecast (WRF v4.0) model (Skamarock and Klemp, 2008)  
169 and the Community Multiscale Air Quality Modeling System (CMAQ v5.0.2) (Byun  
170 and Schere, 2006) were applied to simulate meteorological conditions and atmospheric  
171 chemistry, respectively. WRF simulations were conducted with a 27-km horizontal  
172 resolution, covering the entire mainland China on a grid of  $225 \times 165$  cells (Figure 1).  
173 The CMAQ model was run over the same domain, but with a removal of three grid cells  
174 on each side of the WRF domain. The vertical settings in WRF and CMAQ was the  
175 same as Feng et al. (2020). To account for the rapid expansion of urbanization, we  
176 updated underlying surface information for urban and built-up land using the MODIS  
177 Land Cover Type Product (MCD12C1) Version 6.1 of 2022. Chemical lateral boundary  
178 conditions for NO, NO<sub>2</sub>, HCHO, and O<sub>3</sub> were extracted from the output of the global  
179 CTM (i.e., the Whole Atmosphere Community Climate Model<sub>2</sub> (WACCM) with a  
180 resolution of  $0.9^\circ \times 1.25^\circ$  at 6-hour intervals (Marsh et al., 2013). Meanwhile, boundary  
181 conditions for the other NMVOCs were obtained directly from background profiles. In  
182 the first data assimilation (DA) window, chemical initial conditions (excluding  
183 NMVOCs) were also derived/originated from the WACCM outputs, whereas in  
184 subsequent windows, they were derived through forward simulation using optimized  
185 emissions from the previous window. Table S1 lists the detailed physical and chemical  
186 configurations. To assess the impact of updated NMVOC emissions on O<sub>3</sub> production  
187 efficiency, we further decoupled the contribution of the primary chemical processes to  
188 the O<sub>3</sub> levels using the CMAQ Integrated Reaction Rate (IRR) analysis.

189

## 190 2.1.2 EnKF Assimilation Algorithm

191 The emissions are constrained using the Ensemble Square Root Filter (EnSRF)  
192 algorithm introduced by Whitaker and Hamill (2002). This approach fully accounts for  
193 temporal and geographical variations in both the transportation and chemical reactions  
194 within the emission estimates. During the forecast step, the background ensembles are  
195 derived by applying perturbation to the prior emissions. The perturbed samples are  
196 typically drawn from Gaussian distributions with a mean of zero and a standard  
197 deviation equal to the prior emission uncertainty in each grid cell. Ensemble runs of the  
198 CMAQ model were subsequently performed to propagate the background errors with  
199 each ensemble sample of state vectors.

200 In the analysis step, the ensemble mean  $\overline{\mathbf{X}^a}$  of the analyzed state is regarded as the best  
201 estimate of emissions, which is obtained by updating the background ensemble mean  
202 through the following equations:

$$203 \quad \overline{\mathbf{X}^a} = \overline{\mathbf{X}^b} + \mathbf{K}(\mathbf{y} - \mathbf{H}\overline{\mathbf{X}^b}) \quad (1)$$

$$204 \quad \mathbf{K} = \mathbf{P}^b \mathbf{H}^T (\mathbf{H} \mathbf{P}^b \mathbf{H}^T + \mathbf{R})^{-1} \quad (2)$$

205 where  $\mathbf{y}$  is the observational vector;  $\mathbf{H}$  represents the observation operator mapping  
206 model space to observation space; The expression  $\mathbf{y} - \mathbf{H}\overline{\mathbf{X}^b}$  quantifies the disparities  
207 between simulated and observed concentrations;  $\mathbf{P}^b \mathbf{H}^T$  illustrates how uncertainties in  
208 emissions relate to uncertainties in simulated concentrations; The Kalman gain matrix  
209  $\mathbf{K}$ , dependent on background error covariance  $\mathbf{P}^b$  and observation error covariance  $\mathbf{R}$ ,  
210 determines the relative contributions to the updated analysis.

211 State variables for emissions include  $\text{NO}_x$  and NMVOCs. To reduce the degree of  
212 freedom in the analysis and avoid the difficulty associated with estimating spatio-  
213 temporal variations in background errors for individual species, we focus on optimizing  
214 the lumped total NMVOC emissions. During the forecast step, we differentiate  
215 individual NMVOC species emissions from the total NMVOC emissions using bottom-  
216 up statistical information. For a consistent comparison between simulations and  
217 observations, model-simulated  $\text{NO}_2$  were diagnosed at the time and location of surface  
218  $\text{NO}_2$  measurements, whereas model-simulated HCHO was horizontally sampled to  
219 align with TROPOMI HCHO VCD retrievals, and subsequently integrated vertically.

220 In this study, the DA window was set to one day and daily TROPOMI HCHO columns  
221 were utilized as observational constraints in our inversion framework. The ensemble  
222 size was set to 50 to strike a balance between computational cost and inversion accuracy.  
223 To reduce the impact of unrealistic long-distance error correlations, the Gaspari and  
224 Cohn function (Gaspari and Cohn, 1999) was utilized as covariance localization to  
225 ensure the meaningful influence of observations on state variables within a specified  
226 cutoff radius, while mitigating their negative impacts on distant state variables. The  
227 optimal localization scale is interconnected with factors such as the assimilation  
228 window, the dynamic system, and the lifetime of chemical species. Given the average  
229 wind speed of 2.8 m/s (Table S2) and a DA window of 1 day, the localization scales for  
230 NO<sub>2</sub> and HCHO, both characterized as highly reactive species with lifespans of just a  
231 few hours, were set to 150 km and 100 km, respectively.

## 232 2.2 Observation Data and Errors

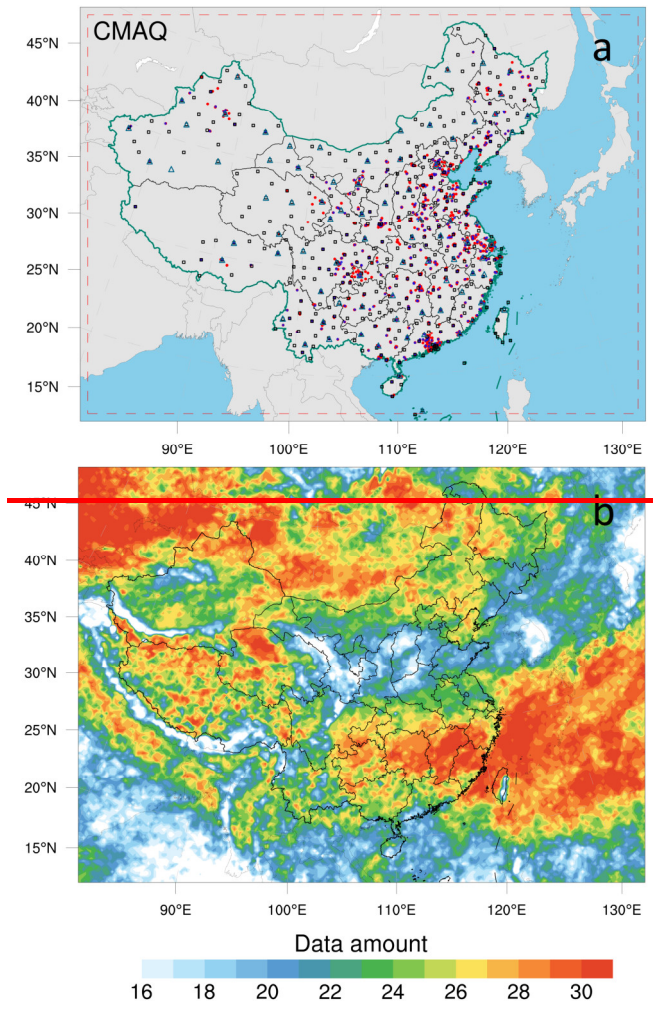
233 Considering the availability of HCHO data, we utilized daily offline retrievals of  
234 tropospheric HCHO columns from Sentinel-5P (S5P) L3 TROPOMI data obtained  
235 through Google Earth Engine (De Smedt et al., 2018). The S5P satellite follows a near-  
236 polar sun-synchronous orbit at an altitude of 824 km with a 17-day repeating cycle. It  
237 crosses the Equator at 13:30 local solar time (LST) on the ascending node. The spatial  
238 resolution at nadir was refined to  $3.5 \times 5.5 \text{ km}^2$  on 6 August 2019. Following the  
239 recommendations in the S5P HCHO product user manual, we filtered the source data  
240 to exclude pixels with qa\_value less than 0.5 for HCHO column number density and  
241 0.8 for aerosol index (AER\_AI). The remaining high-quality pixels with minimal  
242 snow/ice or cloud interference are averaged to 27-km grids. Figure 1b illustrates the  
243 coverage and data amount of TROPOMI HCHO retrievals in August 2022 after  
244 processing. Although the distribution of filtered data exhibits spatial non-uniformity,  
245 most grid cells have observational coverage for over half of the time, particularly in the  
246 southern region of China where NMVOC emissions are higher. ~~We assigned~~  
247 ~~measurement errors of 30% to TROPOMI HCHO columns b~~Based on validation  
248 against a global network of 25 ground-based Fourier transform infrared (FTIR) column  
249 measurements (Vigouroux et al., 2020), TROPOMI HCHO overestimates by 25%  
250 (<math>2.5 \times 10^{15} \text{ molec cm}^{-2}</math>) in clean regions and underestimates by 30% (>=8×10<sup>15</sup> molec  
251 cm<sup>-2</sup>) in polluted regions. Therefore, we set the measurement error to 30%. To evaluate  
252 the effect of observational data retrieval errors on emission estimates, we conducted a

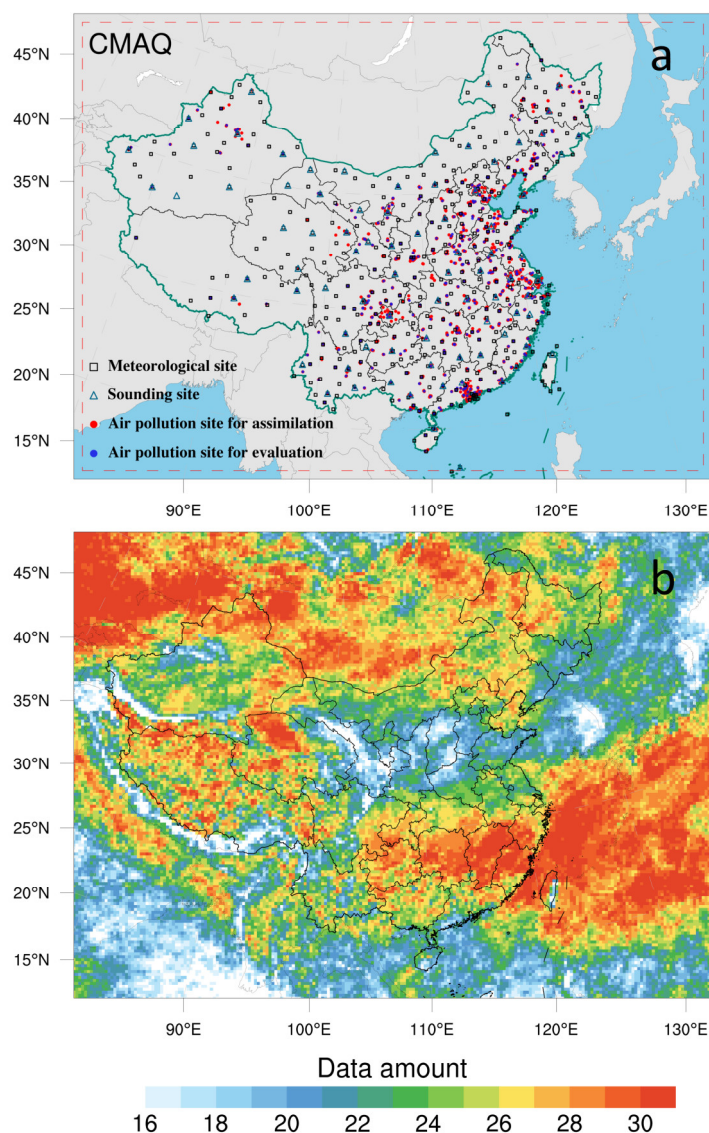


253 sensitivity experiment in which HCHO columns were empirically bias-corrected  
254 according to the error characteristics described above (Figure S1). The posterior  
255 emissions increased by 12.8% compared to those in the base experiment (EMDA),  
256 indicating that the existing retrieval error in HCHO measurements likely exerts an  
257 influence on the estimation of NMVOC emissions. –The representation error can be  
258 disregarded because the model's resolution significantly surpasses that of the  
259 TROPOMI pixels.

260 To address the chemical feedback among VOC-NO<sub>x</sub>-O<sub>3</sub>, we also simultaneously  
261 optimized NO<sub>x</sub> emissions by assimilating in-situ NO<sub>2</sub> observations. The extensively  
262 covered and high-precision monitoring network can provide sufficient constraints for  
263 emission inversion (Figure 1a). Hourly averaged surface NO<sub>2</sub> observations from  
264 national control air quality stations obtained from the Ministry of Ecology and  
265 Environment of the People's Republic of China (<http://106.37.208.228:8082/>, last  
266 access: 5 May 2023). In case where multiple stations are located within the same grid,  
267 a random site is chosen for validation, while the remaining sites are averaged to mitigate  
268 the impact of error correlation (Houtekamer and Zhang, 2016) for assimilation. In total,  
269 1276 stations were chosen for assimilation and an additional 425 independent stations  
270 were selected for verification (Figure 1a). The observation error covariance matrix **R**  
271 incorporates contributions from both measurement and representation errors. The  
272 measurement error is defined as  $\varepsilon_0 = 1.0 + 0.005 \times \Pi_0$ , where  $\Pi_0$  represents the  
273 observed NO<sub>2</sub> concentration. Following the approach of Elbern et al. (2007) and Feng  
274 et al. (2018), the representative error is defined as  $\varepsilon_r = \gamma \varepsilon_0 \sqrt{\Delta l / L}$ , where  $\gamma$  is a tunable  
275 parameter (here,  $\gamma=0.5$ ),  $\Delta l$  is the grid spacing (27 km), and  $L$  is the radius (here,  $L=0.5$ )  
276 of the observation's influence area. The total observation error ( $r$ ) was defined as  $r =$   
277  $\sqrt{\varepsilon_0^2 + \varepsilon_r^2}$ . The observation errors are assumed to be uncorrelated so that **R** is a  
278 diagonal matrix.

279





281

282 **Figure 1.** Model domain and observation network (a) and data amount of TROPOMI  
 283 HCHO retrievals during August 2022 in each grid (b). The red dashed frame delineates  
 284 the CMAQ computational domain; black squares denote surface meteorological  
 285 measurement sites; navy triangles indicate sounding sites (Text S1), and red and blue  
 286 dots represent air pollution measurement sites, where red dots are used for assimilation  
 287 and blue dots for independent evaluation.

### 288 **2.3 Prior Emissions and Uncertainties**

289 The prior anthropogenic NO<sub>x</sub> and NMVOC emissions for China were obtained from  
 290 the most recent Multi-resolution Emission Inventory for China of 2020 (MEIC,  
 291 <http://www.meicmodel.org/>, last access: 8 May 2023) (Zhang et al., 2009). For  
 292 anthropogenic emissions outside China, we utilized the mosaic Asian anthropogenic  
 293 emission inventory (MIX) for the base year of 2010 (Li et al., 2017b). The daily

294 emission inventory, which was arithmetically averaged from the combined monthly  
295 emission inventory, was employed as the first guess. Ship emissions were derived from  
296 the shipping emission inventory model (SEIM) for 2017, which was calculated based  
297 on the observed vessel automatic identification system (Liu et al., 2017). Biomass  
298 burning emissions were retrieved from the Global Fire Emissions Database version 4.1  
299 (GFEDv4, <https://www.globalfiredata.org/>, last access: 8 May 2023) (van der Werf et  
300 al., 2017; Mu et al., 2011). Biogenic NO<sub>x</sub> and NMVOC emissions were calculated using  
301 the Model of Emissions of Gases and Aerosols from Nature (MEGAN) developed by  
302 Guenther et al. (2012).

303 As previously mentioned, the optimized emissions are transferred to the next DA  
304 window as prior emissions for iterative inversion. For biogenic emissions, it is  
305 decomposed into hourly scales based on the daily varying temporal profiles in MEGAN  
306 as model inputs. Daily emission variations will largely dominate the uncertainty in  
307 emissions. Taking into account compensating for model errors and avoiding filter  
308 divergence, we consistently applied an uncertainty of 25% to each model grid of NO<sub>x</sub>  
309 emissions at each DA window, as in Feng et al. (2020). NMVOC emissions typically  
310 exhibit greater uncertainties compared to NO<sub>x</sub> emissions (Li et al., 2017b). Based on  
311 model evaluation, the uncertainty of NMVOC emissions was set to 40% (Kaiser et al.,  
312 2018; Sourì et al., 2020; Cao et al., 2018). A sensitivity experiment involving a doubling  
313 of the prior uncertainty (80%) revealed that the differences in posterior NMVOC  
314 emissions amounted to a mere 0.2% (Figure S2). The implementation of a ‘two-step’  
315 inversion strategy allows for the timely correction of residual errors from the previous  
316 assimilation window in the current window, thus ensuring that the RAPAS system has  
317 a relatively low dependence on prior uncertainty settings. This study also addresses  
318 uncertainties in emissions for CO, SO<sub>2</sub>, primary PM<sub>2.5</sub>, and coarse PM<sub>10</sub> to consider the  
319 chemical feedback between different species following Feng et al. (2023).

### 320 **3 Experimental Design**

321 During the summer of 2022, southern China experienced severe heatwave conditions.  
322 The combination of high temperatures and drought had a pronounced effect on  
323 vegetation growth and NMVOC emissions, thereby influencing O<sub>3</sub> production (Wang  
324 et al., 2023). Consequently, we opted to focus on August 2022, as it presented an ideal  
325 period for testing the capabilities of our DA system. Before implementing the emission  
326 inversion, a relatively perfect initial field is generated at 0000 UTC on August 01 2022

327 through conducting a 5-day simulation with 6-hour interval 3D-Var data assimilation.  
328 Subsequently, daily emissions are continuously updated over the entire month of  
329 August (EMDA). Additionally, we designed a sensitivity experiment (EMS) to illustrate  
330 the significance of optimizing NO<sub>x</sub> emissions in quantifying VOC-O<sub>3</sub> chemical  
331 reactions. In this experiment, NO<sub>x</sub> emissions were not optimized. To validate the  
332 posterior emissions of NO<sub>x</sub> and NMVOCs in EMDA, we compared two parallel  
333 forward simulation experiments with NO<sub>2</sub> and HCHO measurements, denoted as CEP  
334 and VEP, corresponding to prior and posterior emission scenarios, respectively, against  
335 NO<sub>2</sub> and HCHO measurements. To investigate the impact of optimizing NMVOC  
336 emissions on the secondary production and loss of surface O<sub>3</sub>, a forward simulation  
337 experiment (CEP1) was conducted with the prior NMVOC emissions and the posterior  
338 NO<sub>x</sub> emissions. ~~Additionally, we designed three sensitivity experiments to investigate~~  
339 ~~the robustness of the constrained NMVOC emissions. EMS1 involved doubling the~~  
340 ~~background error from 40% to 80% to investigate the influence of background error~~  
341 ~~settings. EMS2 aimed to evaluate the effect of observational data retrieval errors on~~  
342 ~~emission estimates, in which HCHO columns were empirically bias corrected based on~~  
343 ~~error characteristics (Souri et al., 2021). EMS3 aimed to illustrate the significance of~~  
344 ~~optimizing NO<sub>x</sub> emission in quantifying VOC-O<sub>3</sub> chemical reactions. In this~~  
345 ~~experiment, NO<sub>x</sub> emissions were not optimized. Two~~ Another forward modelling  
346 experiments (CEP2 ~~and CEP3~~) were also performed using the posterior emissions  
347 of EMS2 ~~and EMS3~~ to evaluate their performance. All experiments employ identical  
348 meteorological fields, as well as the same gas-phase and aerosol modules. Table 1  
349 summarizes the different emission inversion and validation experiments conducted in  
350 this study.

351

352

353

354

355

356

357

358

359 **Table 1.** The assimilation, sensitivity, and validation experiments conducted in this  
 360 study.

Exp.Type	Exp. Name	NMVOC emissions	NO <sub>x</sub> emissions	Assimilated HCHO retrievals
Assimilation	EMDA	MEIC 2020 and MEGAN for August (the first DA window), optimized emissions of the previous window (other DA windows)	MEIC 2020 and MEGAN for August (the first DA window), optimized emissions of the previous window (other DA windows)	Default
	EMS1	<del>Same as EMDA but with doubled default uncertainty</del>	Same as EMDA	Default
Sensitivity	EMS2	Same as EMDA	Same as EMDA	<del>Reduce by 25% in regions with observations <math>&lt; 2.5 \times 10^{15}</math> molec <math>\text{cm}^{-2}</math> and increase by 30% in regions with observations <math>&gt; 8 \times 10^{15}</math> molec <math>\text{cm}^{-2}</math></del>
	EMS3	Same as EMDA	MEIC 2020 and MEGAN for August	Default
Validation	CEP	MEIC 2020 and MEGAN for August	MEIC 2020 and MEGAN for August	↓
	VEP	Posterior emissions of EMDA	Posterior emissions of EMDA	↓
	CEP1	Same as CEP	Posterior emissions of EMDA	↓
	CEP2	<del>Posterior emissions of EMS2</del>	<del>Posterior emissions of EMS2</del>	↓
	<del>CEP3</del> CEP23	Posterior emissions of EMS3	Same as CEP	↓

## 361 4 Results

### 362 4.1 Inverted Emissions

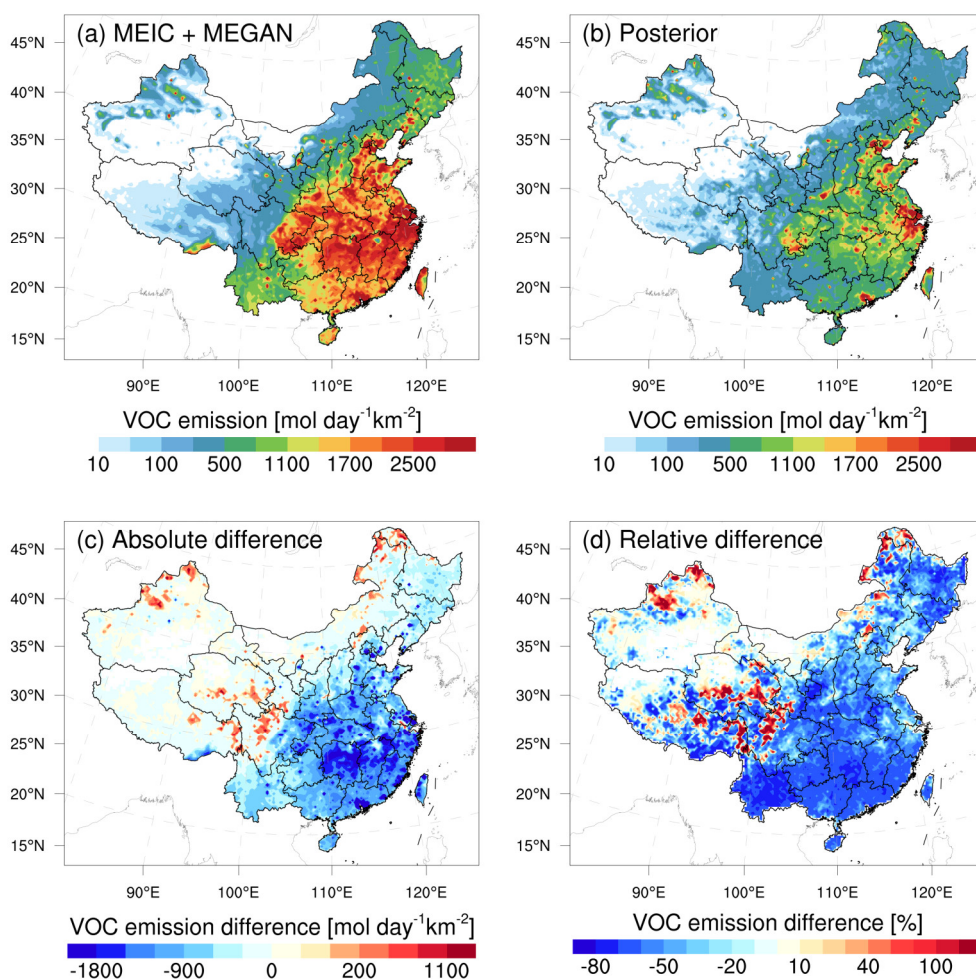
363 Figure 2 shows the spatial distribution of temporally averaged prior and posterior  
 364 NMVOC emissions, along with their differences, in NMVOC emissions. Hotspots of  
 365 prior NMVOC emissions were prevalent across much of central and southern China.  
 366 However, posterior NMVOC emissions were predominantly concentrated in the NCP,  
 367 Yangtze River Delta (YRD), PRD, and Sichuan Basin (SCB), characterized by high  
 368 levels of anthropogenic activity. High emissions are also located in parts of central and  
 369 southern China with warm climate favorable for emitting biogenic NMVOCs.  
 370 Employing TROPOMI HCHO observations as constraints led to widespread decreases



371 of approximately 60–70% over these areas, indicating a large substantial of biogenic  
372 NMVOC emissions. In northwestern China, there was a moderate increase in NMVOC  
373 emissions. A potential significant TROPOMI retrieval errors bias in polluted regions  
374 could exacerbate the emission ~~reduction~~ decreases (Text S2). Additionally, uncertainties  
375 in MEGAN parameterization have significant implications for NMVOC emission  
376 estimations, particularly concerning the responses of vegetation in MEGAN to  
377 temperature and drought stress (Angot et al., 2020; Jiang et al., 2018). Zhang et al.  
378 (2021) highlighted that the temperature-dependent activity factor noticeably increases  
379 with rising temperatures in MEGAN. Wang et al. (2021b) pointed out that the missing  
380 of a drought scheme is one of the factors causing the overestimation of isoprene  
381 emissions in MEGAN. Opacka et al. (2022) optimized the empirical parameter in the  
382 MEGANv2.1 soil moisture stress algorithm, resulting in significant reductions in  
383 isoprene emissions and providing better agreement between modelled and observed  
384 HCHO temporal variability in the central U.S. These findings demonstrate that  
385 uncertainties in MEGAN parameterization also have significant implications for  
386 NMVOC emission modeling.

387 During the study period, China experienced severe heatwave conditions, which may  
388 further hinder the MEGAN's ability to effectively capture the impacts of high  
389 temperatures and drought on vegetation, thus resulting in significant overestimation in  
390 NMVOC emissions (Wang et al., 2022). Nevertheless, the large magnitude of emission  
391 reductions of 50.2% in our inversion is comparable to studies in southern China  
392 (Bauwens et al., 2016; Zhou et al., 2023), southeastern US (Kaiser et al., 2018), Africa  
393 (Marais et al., 2014), India (Chaliyakunnel et al., 2019), Amazonia (Bauwens et al.,  
394 2016), and parts of Europe (Curci et al., 2010), but opposite to the large-scale emission  
395 increase over China in Cao et al. (2018). For NO<sub>x</sub> (Figure S34), the nationwide total  
396 emissions decreased by 10.2%, with the main reductions concentrated in the NCP, YRD,  
397 parts of Central China, and most key urban areas.

398



399

400 **Figure 2.** Spatial distribution of the time-averaged (a) prior emissions (MEIC 2020 +  
 401 **MEEMGAN**), (b) posterior emissions, (c) absolute difference (posterior minus prior),  
 402 and (d) relative difference of NMVOCs over China.

403 Table 2 shows the changes in emissions of biogenic NMVOCs across different land  
 404 cover types (Figure S42) after inversion. The most significant reduction in biogenic  
 405 emissions occurred within woody savannas, accounting for 26.9% of the overall  
 406 reduction, followed by savannas and croplands, accounting for 21.2% and 17.2%  
 407 respectively. Among all vegetation types, the broadleaf evergreen forests, recognized  
 408 as the primary source of isoprene emission (Wang et al., 2021a), presented the greatest  
 409 uncertainty, with NMVOC emissions experiencing a significant reduction of 66.2%.  
 410 Standard emission rates in MEGAN are derived from leaf- or canopy-scale flux  
 411 measurements and extrapolated globally across regions sharing similar landcover  
 412 characteristics, based on very limited observations (Guenther et al., 1995). This  
 413 methodology introduces biases due to the large variability in emission rates among  
 414 plant species. ~~Opacka et al. (2022) optimized the empirical parameter in the~~



415 ~~MEGANv2.1 soil moisture stress algorithm, resulting in significant reductions in~~  
 416 ~~isoprene emissions and providing better agreement between modelled and observed~~  
 417 ~~HCHO temporal variability in the central U.S. These findings demonstrate that~~  
 418 ~~uncertainties in MEGAN parameterization also have significant implications for~~  
 419 ~~NMVOC emission modeling.~~

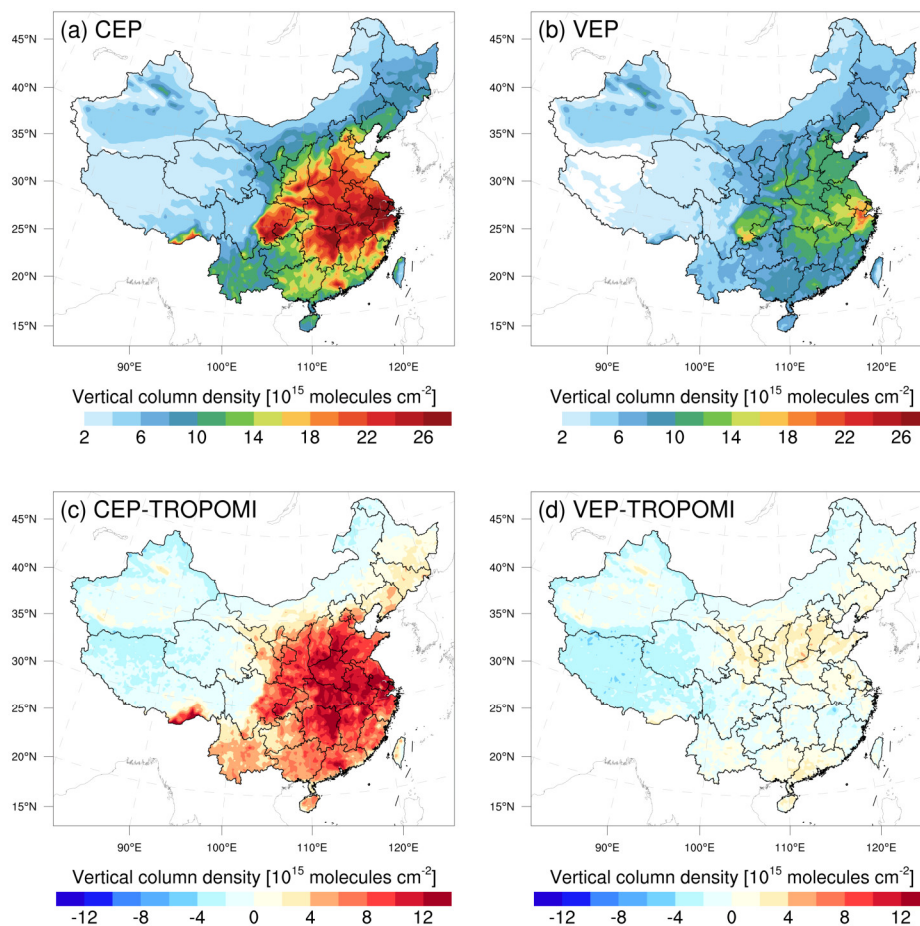
420 **Table 2.** Prior and posterior biogenic NMVOC emissions, as well as their differences  
 421 for different land cover types.

Land cover type	Prior	Posterior	Difference
	Mmol/month	Mmol/month	Mmol/month (%)
Evergreen needleleaf forests	955.7	549.3	-406.4 (-42.5)
Evergreen broadleaf forests	13985.1	4728.2	-9256.8 (-66.2)
Deciduous needleleaf forests	46.6	48.8	2.2 (4.7)
Deciduous broadleaf forests	8335.5	3487.4	-4848.1 (-58.2)
Mixed forests	8731.0	3961.7	-4769.4 (-54.6)
Closed shrublands	9.7	3.7	-6.0 (-61.5)
Open shrublands	21.3	8.6	-12.8 (-59.8)
Woody savannas	39327.2	16925.2	-22402.0 (-57.0)
Savannas	28319.7	10629.4	-17690.3 (-62.5)
Grasslands	16912.7	14269.6	-2643.1 (-15.6)
Permanent wetlands	286.1	115.4	-170.8 (-59.7)
Croplands	25537.8	11215.5	-14322.2 (-56.1)
Cropland-natural vegetation mosaics	10894.7	4289.8	-6605.0 (-60.6)
Sparsely vegetated	1814.7	1644.0	-170.6 (-9.4)

422 **4.2 Evaluations for Posterior Emissions**

423 The NO<sub>x</sub> emissions were first evaluated by indirectly comparing the forward simulated  
 424 NO<sub>2</sub> concentrations with measurements. As shown in Figure S53, the CEP with prior  
 425 emissions exhibited positive biases in eastern China and negative biases in western  
 426 China. However, when posterior emissions were used in the VEP, a substantial  
 427 improvement in simulation performance was observed. Biases were limited to within  
 428  $\pm 3 \mu\text{g m}^{-3}$ , and correlation coefficients exceeded 0.7 across the entire region. Figure 3

429 presents the simulated HCHO VCDs using prior and posterior NMVOCs emissions,  
 430 along with their associated biases. Both experiments showed high VCDs over central  
 431 and eastern China, especially in the YRD and SCB. However, the CEP displayed  
 432 substantial overestimation across most of mainland China, with the largest bias  
 433 reaching  $12 \times 10^{15}$  molec  $\text{cm}^{-2}$  in Central China. Conversely, the VEP demonstrated  
 434 notable improvements in both the magnitude and spatial distribution of simulated  
 435 HCHO columns after the inversion compared to TROPOMI retrievals. More than 84%  
 436 of the areas exhibited biases of less than  $1 \times 10^{15}$  molec  $\text{cm}^{-2}$ , and no significant spatial  
 437 variation was observed. Overall, the biases in simulated HCHO VCDs decreased by  
 438 75.7% after the inversion. These results emphasize the efficiency of our system in  
 439 reducing uncertainty in both  $\text{NO}_x$  and NMVOC emissions.



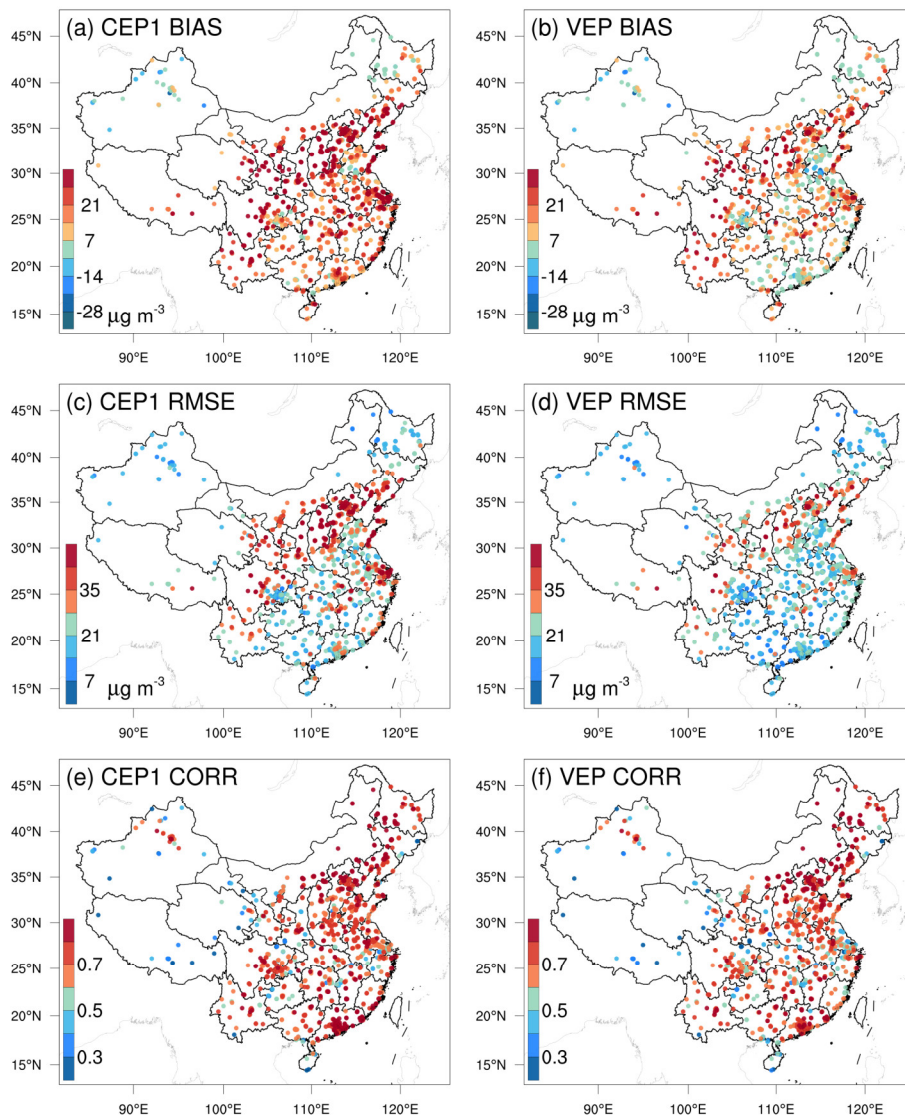
440

441 **Figure 3.** Simulated HCHO vertical column densities using prior (a) and posterior (b)  
 442 NMVOC emissions, along with their biases (c and d) against TROPOMI measurement.  
 443 All model results were sampled at TROPOMI overpass time.

444 **4.3 Implications for Surface  $\text{O}_3$**

445 Figure 4 shows the spatial distribution of the mean bias (BIAS), root mean square error  
446 (RMSE), and correlation coefficient (CORR) for simulated O<sub>3</sub> concentrations in the  
447 CEP1 and VEP experiments compared to assimilated observations. Beyond the  
448 northwestern region of China, the CEP1 exhibited significant overestimation  
449 throughout the entire area, with a BIAS of 20.5 μg m<sup>-3</sup>. ~~By intercomparing 14 state-of-~~  
450 ~~the-art CTMs with O<sub>3</sub> observations within the framework of the MICS-Asia III, Li et~~  
451 ~~al. (2019) identified a substantial overestimation of annual surface O<sub>3</sub> in East Asia,~~  
452 ~~ranging from 20 to 60 μg m<sup>-3</sup>. Notably, the NCP exhibited substantial overestimations,~~  
453 ~~with most models overestimating O<sub>3</sub> by 100–200% during May–October.~~ In the VEP,  
454 the modeled O<sub>3</sub> chemical production were alleviated, especially in the southern regions  
455 of China where NMVOC emissions had significantly decreased. Overall, observation-  
456 constrained NMVOC emissions resulted in a 49.3% decrease in the BIAS, bringing it  
457 down to 10.4 μg m<sup>-3</sup>. Additionally, the RMSE showed noticeable improvement due to  
458 the assimilation of HCHO observation, reducing the value from 30.9 to 23.3 μg m<sup>-3</sup>.  
459 Despite a significant reduction in NMVOC emissions after inversion, notable  
460 overestimations persisted in northern provinces such as Liaoning, Hebei, Shanxi, and  
461 Shaanxi. This may be attributed to limited NMVOC constraints resulting from  
462 insufficient observations during the study period (Figures 1b and 3d). The remaining  
463 discrepancies between simulations and observations can be attributed to the combined  
464 results of intricate urban-rural sensitivity regimes and O<sub>3</sub> photochemistry reactions,  
465 which may not be comprehensively represented by CMAQ model, masking any  
466 potential improvement expected from the constrained emissions (See Sect. 4.4). The  
467 CORR was comparable between the CEP1 and VEP experiments, reflecting that the  
468 CMAQ model effectively simulated the temporal variation of O<sub>3</sub> concentrations. The  
469 biases at the independent sites were similar to those at the assimilated sites (Figure S64).  
470 In comparison to CEP1, the decreasing ratios in BIAS and RMSE in VEP were 46.7%  
471 and 23.4%, respectively.

472



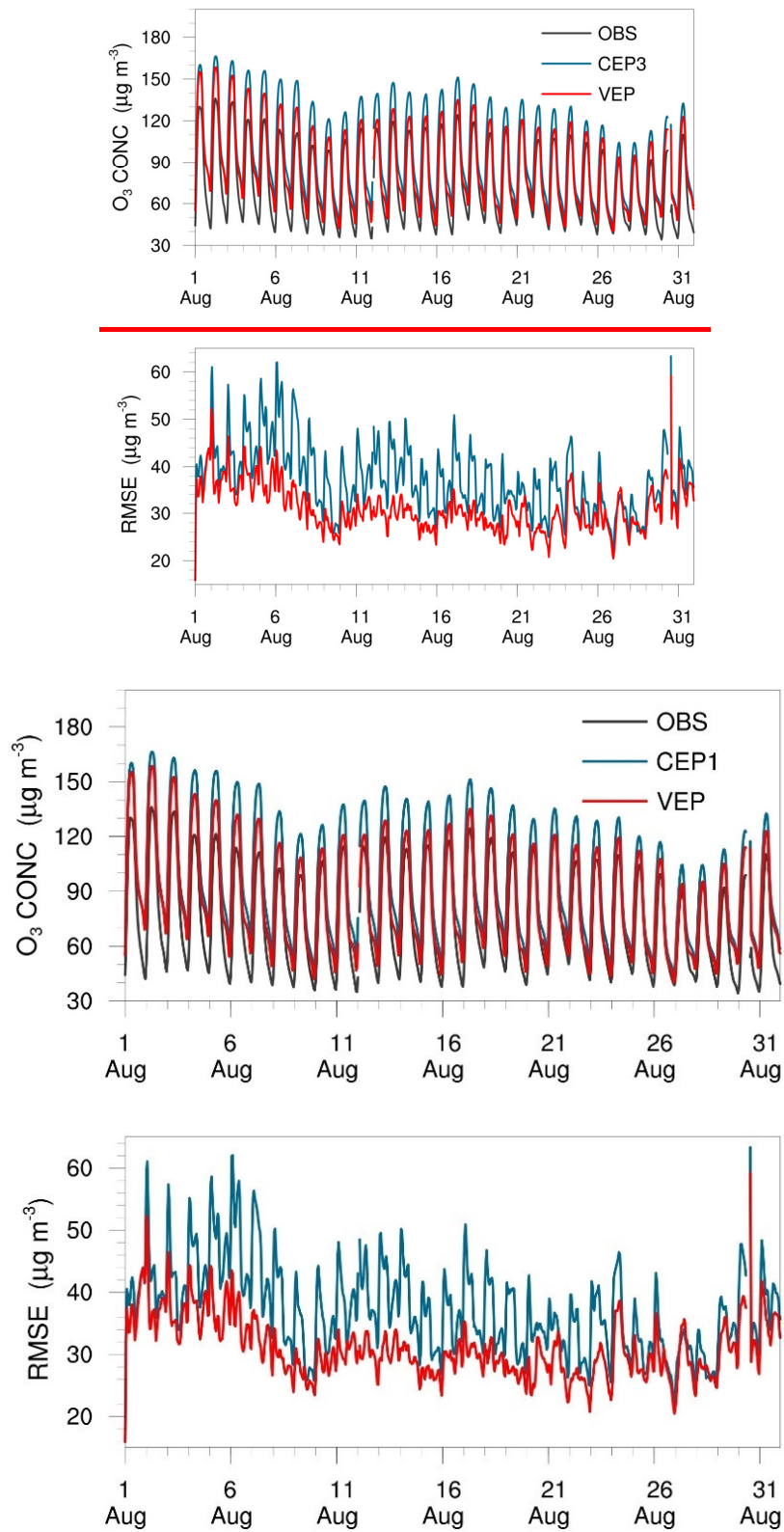
473

474 **Figure 4.** Spatial distribution of mean bias (BIAS, a and b), root mean square error  
 475 (RMSE, c and d), and correlation coefficient (CORR, e and f) for simulated O<sub>3</sub> using  
 476 prior (left, CEP1) and posterior (right, VEP) emissions, respectively, against  
 477 assimilated observations.

478 Figure 5 shows the time series of simulated and observed hourly O<sub>3</sub> concentrations and  
 479 their RMSEs, verified against surface monitoring sites. The VEP achieved better  
 480 representations of diurnal O<sub>3</sub> variations compared with those in the CEP1, especially  
 481 excelling in reproducing elevated O<sub>3</sub> concentrations at noon. Constraining the NMVOC  
 482 emissions also led to better model simulations in terms of RMSE throughout the entire  
 483 study period. Overall, the assimilation of HCHO column observations effectively  
 484 reduced NMVOC emission uncertainties and consequently improved simulations of

485 HCHO and O<sub>3</sub>. These improvements hold promise for further research into the  
486 implications of emission optimizations on regional O<sub>3</sub> photochemistry.

487

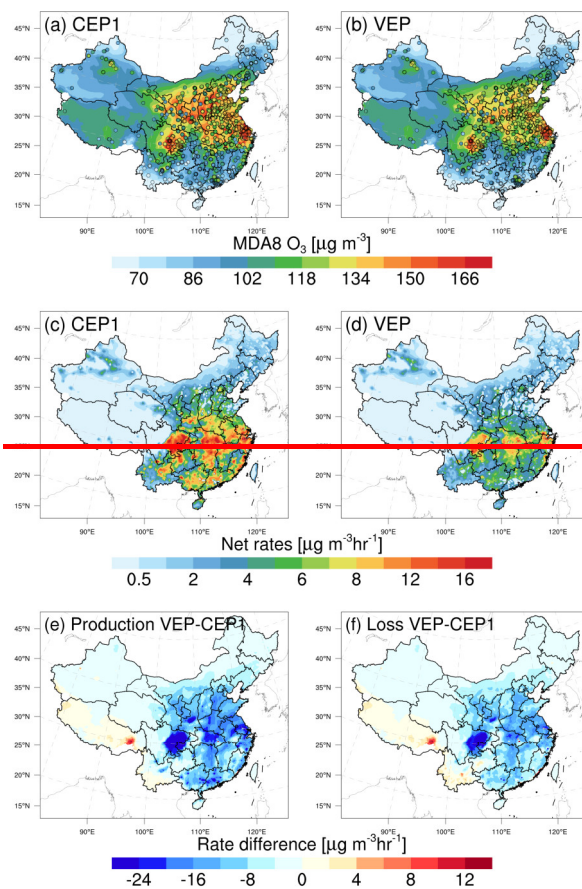


488

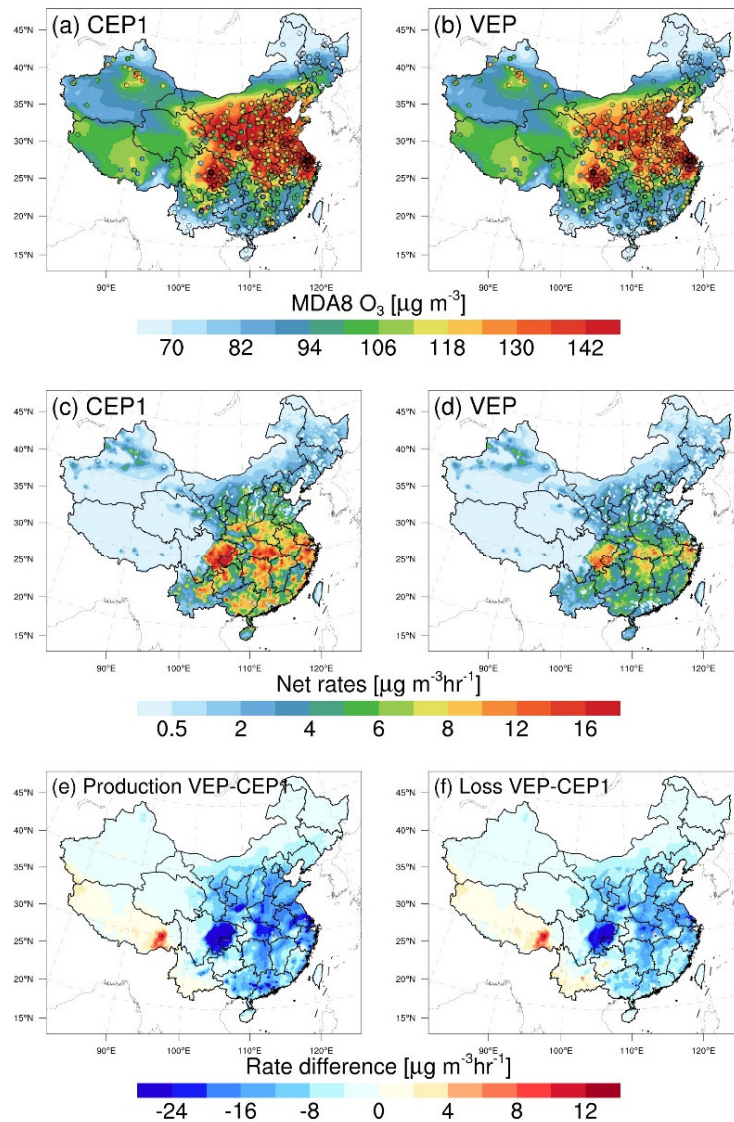
489 **Figure 5.** Time series comparison of hourly surface O<sub>3</sub> concentrations (μg m<sup>-3</sup>) and  
490 RMSE (μg m<sup>-3</sup>) from CEP1 and VEP experiments against all observations.



491 As crucial O<sub>3</sub> precursors, the abundance of NMVOCs plays a significant role in  
 492 modulating O<sub>3</sub> production. Here we employed the IRRs to elucidate changes related to  
 493 O<sub>3</sub> production and loss at the surface, stemming from constrained NO<sub>x</sub> and NMVOC  
 494 emissions. Figure 6 illustrates comparisons of the simulated maximum daily 8-hour  
 495 average (MDA8) surface O<sub>3</sub> levels and net reaction rates before and after the inversion.  
 496 The CEP1 exhibited an overestimation of O<sub>3</sub> levels, with a BIAS of 22.6% compared  
 497 to observed O<sub>3</sub> concentrations. This overestimation corresponded to the high net  
 498 chemical rates of O<sub>3</sub> in these areas (Figure S75). After inversion, O<sub>3</sub> net rates mitigated  
 499 in most regions. Consequently, the VEP experiment yielded results that closely aligned  
 500 with observations, with a BIAS of 9.2%. Referring to Figure 6e and 6f, differences in  
 501 production rates of O<sub>3</sub> closely track the changes in the NMVOC emissions (Figure 2).  
 502 The discrepancies in specific regions may be attributed to the complex nonlinear  
 503 relationships associated with O<sub>3</sub> and its precursors, which depend on prevailing  
 504 chemical regimes and regional transport. Additionally, changes in O<sub>3</sub> production  
 505 predominantly drive the overall decrease in O<sub>3</sub> concentrations, outweighing changes in  
 506 O<sub>3</sub> loss.



507



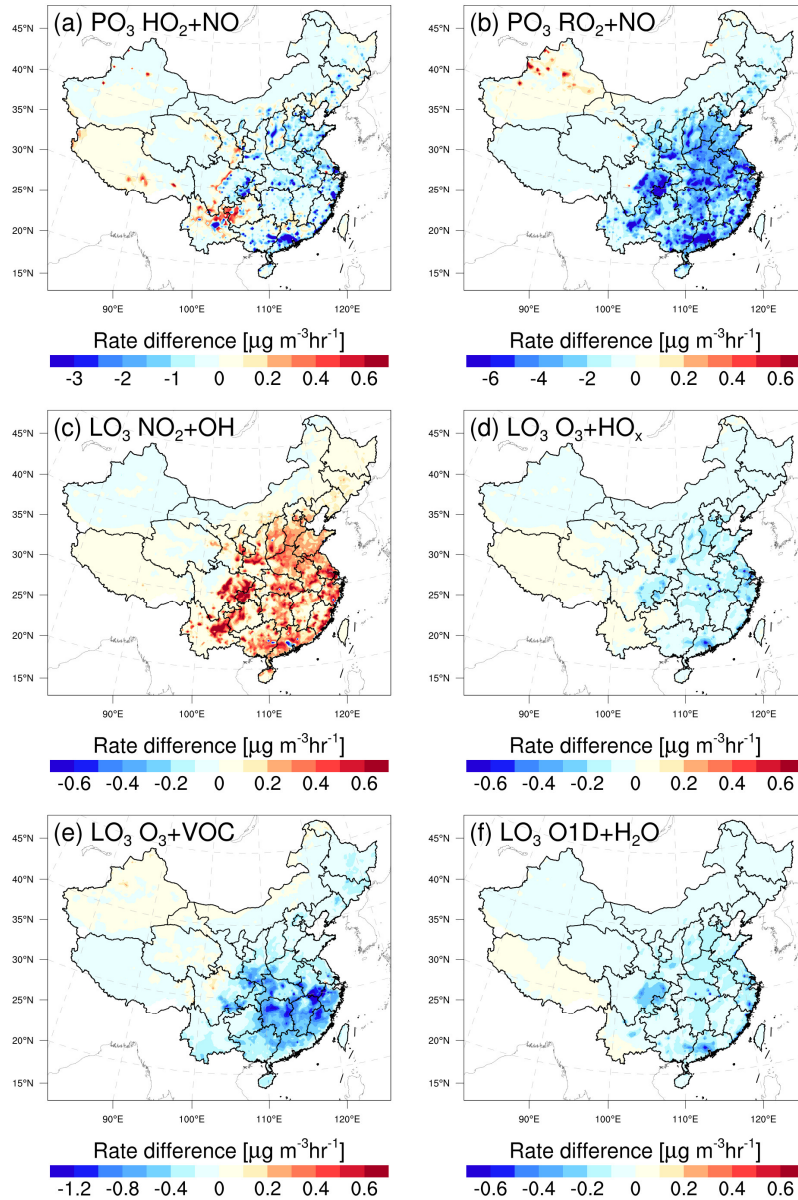
508

509 **Figure 6.** Comparisons of (a, b) simulated maximum daily 8-hour average (MDA8) O<sub>3</sub>  
 510 concentrations, (c, d) net reaction rates, (e, f) and differences in production and loss  
 511 rates between CEP1 and VEP experiments at the surface. Surface MDA8 O<sub>3</sub> values  
 512 (circles) from the national control air quality stations were overlaid

513 Figure 7 shows the differences in the six principal pathways responsible for O<sub>3</sub> loss and  
 514 formation, when comparing simulations employing prior and posterior emissions. The  
 515 reactions of HO<sub>2</sub> + NO and RO<sub>2</sub> + NO are treated as the pathways leading to O<sub>3</sub>  
 516 formation, whereas O<sub>3</sub> loss involves reactions including NO<sub>2</sub> + OH, O<sub>3</sub> + HO<sub>2</sub>, O<sub>3</sub> +  
 517 NMVOCs, and O<sub>1</sub>D + H<sub>2</sub>O (Wang et al., 2019). Our analysis was focused on the time  
 518 frame from 12:00 to 18:00 according to China standard time (CST). The differences  
 519 were computed by subtracting the simulation with posterior emissions from those with  
 520 prior emissions. Following the emission of NMVOCs, they undergo rapid oxidation by

521 atmospheric hydroxyl (OH) radicals. Due to the substantial decrease in NMVOC  
522 emissions, there was a reduction in the production of hydroperoxy radicals (HO<sub>2</sub>) and  
523 organic peroxy radicals (RO<sub>2</sub>) (Figure S86). Consequently, this reduction in HO<sub>2</sub>/RO<sub>2</sub>  
524 levels, coupled with their reaction with NO, resulted in diminished O<sub>3</sub> production  
525 (Figures 7a and 7b). A strong correlation was observed between changes in O<sub>3</sub>  
526 production via the RO<sub>2</sub> + NO reaction and NMVOC emissions (Figure 2), consistent  
527 with the findings of Sourì et al. (2020). Typically, in NMVOC-rich environments, a  
528 decrease in NMVOC emissions boosts OH concentrations. Consequently, we noted an  
529 enhancement in the NO<sub>2</sub> + OH reaction in the eastern and central regions of China. In  
530 response to heightened HO<sub>x</sub> concentrations over these areas, an increased O<sub>3</sub> loss  
531 through the O<sub>3</sub> + HO<sub>x</sub> pathway was observed. Furthermore, we detected a substantial  
532 decrease in O<sub>3</sub> loss through reactions with NMVOCs, especially in the southern China,  
533 where substantial isoprene emissions are prevalent. This reduction was primarily  
534 attributable to the decrease in NMVOC and O<sub>3</sub> levels. While the NMVOC + O<sub>3</sub> reaction  
535 proceeds at a substantially slower rate NMVOC + OH, this specific chemical pathway  
536 remains significant in oxidizing NMVOC and forming HO<sub>x</sub> in forests areas (Paulson  
537 and Orlando, 1996). The difference in O<sub>1</sub>D + H<sub>2</sub>O is primarily driven by the decrease  
538 of O<sub>3</sub> photolysis. Although the rate of O<sub>3</sub> loss decreases in some chemical pathways,  
539 overall, the rate of O<sub>3</sub> production dominates the changes in O<sub>3</sub> concentration.





540

541 **Figure 7.** Differences in six major pathways of  $\text{O}_3$  production and loss between CEP1  
 542 and VEP experiments at the surface. Time period: August 2022, 12:00–18:00 CST.  $\text{PO}_3$   
 543 and  $\text{LO}_3$  represent the pathways of  $\text{O}_3$  formation and loss, respectively.

544 **4.4 Discussions**

545 [O<sub>3</sub> simulations over China have a tendency to be overestimated in studies involving](#)  
 546 [chemical transport modeling. For example, by intercomparing 14 state-of-the-art CTMs](#)  
 547 [with O<sub>3</sub> observations within the framework of the MICS-Asia III, Li et al. \(2019\)](#)  
 548 [identified a substantial overestimation of annual surface O<sub>3</sub> in East Asia, ranging from](#)  
 549 [20 to 60  \$\mu\text{g m}^{-3}\$ . Notably, the NCP exhibited substantial overestimations, with most](#)  
 550 [models overestimating O<sub>3</sub> by 100–200% during May–October. Despite our](#)

551 optimization of O<sub>3</sub> precursor emissions, the posterior simulations still exhibit some  
552 degree of overestimation (Figure 4), suggesting that there may indeed be an effect of  
553 systematic bias, such as meteorological fields, spatial resolution, model treatments of  
554 nonlinear photochemistry and other physical processes. The WRF can generally  
555 reproduce meteorological conditions sufficiently in terms of their temporal variation  
556 and magnitude over China (Figure S9), with small biases of -0.5 °C, -5.3%, 0.3 m/s,  
557 and -42.4 m for temperature at 2 m, relative humidity at 2 m, and wind speed at 10 m,  
558 and planetary boundary layer height, respectively. However, due to the relatively coarse  
559 spatial resolution, NO titration effects in urban areas may not be well represented in the  
560 model, which can lead to an overestimation of O<sub>3</sub> in these areas. Additionally, model  
561 inherent errors arising from the model structure, parameterization, and the  
562 simplification or lack of chemical mechanisms inevitably affect the O<sub>3</sub> simulations. For  
563 example, Li et al. (2018) reported that heterogeneous reactions of nitrogen compounds  
564 could weaken the atmospheric oxidation capacity and thus reduce surface O<sub>3</sub>  
565 concentration by 20–40 µg m<sup>-3</sup> for the polluted regions over China. These reactions  
566 have not been fully incorporated in CMAQ chemical mechanisms. However, there is  
567 still a lack of reasonable and effective algorithms for addressing model errors through  
568 assimilation (Houtekamer and Zhang, 2016).

569 ~~The prior NMVOC emissions were found to be overestimated relative to the top-down~~  
570 ~~constraints from TROPOMI HCHO retrievals. The results of the top-down inversion~~  
571 ~~may be susceptible to uncertainties related to the inversion configuration and~~  
572 ~~observational data. Particularly, background error settings affect the relative weighting~~  
573 ~~of prior and observation to posterior emissions, which may potentially introduce~~  
574 ~~considerable uncertainty into the spatial patterns and magnitudes of the NMVOC~~  
575 ~~emission inversion. Another critical concern pertains to HCHO retrieval errors.~~  
576 ~~Correcting the low TROPOMI HCHO column biases would result in elevated posterior~~  
577 ~~emissions, while the opposite holds true. To investigate the impact of background error~~  
578 ~~on emission inversion, a sensitivity test (EMS1) was conducted, doubling the~~  
579 ~~background error to 80%. Compared with the base inversion, the sensitivity test~~  
580 ~~produced a noticeable increase in posterior NMVOC emissions in southwestern China,~~  
581 ~~especially in Tibet. In contrast, emissions in eastern China exhibited a slight decrease~~  
582 ~~(Figure S7). This can be expected, as the inversion is more inclined to deviate from the~~  
583 ~~a priori due to decreased confidence. However, at a national scale, the difference~~

584 between the two posterior emissions was nearly negligible. The substantial disparities  
585 over the Tibetan Plateau between the two inversions can be attributed to the horizontal  
586 HCHO inhomogeneity caused by mountain terrain and the relatively low signal to  
587 noise ratio in the TROPOMI satellite data in the background atmosphere (Cheng et al.,  
588 2023), resulting in the inclusion of more outliers in the inversion (Su et al., 2020).  
589 Nevertheless, the discrepancies in NMVOC emission estimates amounted to a mere  
590 0.2%, suggesting that the posterior emission estimates were not largely affected by the  
591 background error setting. This can be primarily attributed to the superiority of the 'two-  
592 step' inversion strategy employed within the RAPAS system.

593 Due to the spatiotemporal variability in retrieval errors, directly incorporating  
594 observations into an inversion system remains a challenging task. Based on the biases  
595 outlined in Vigouroux et al. (2020), another sensitivity test (EMS2) addressed the  
596 existing biases in TROPOMI HCHO by reducing measurements by 25% ( $<2.5 \times 10^{15}$   
597 molec  $\text{cm}^{-2}$ ) in clean regions and increasing them by 30% ( $\geq 8 \times 10^{15}$  molec  $\text{cm}^{-2}$ ) in  
598 polluted regions. Figure 8 shows that bias-corrected HCHO columns resulted in a slight  
599 decrease in NMVOC emissions in the low pollution regions of western China, whereas  
600 emissions increased in the high pollution regions of eastern and central China,  
601 particularly in the SCB and the vicinity of the YRD. In comparison to the EMDA  
602 experiment, the posterior emissions from EMS1 increased by 12.8% (decreased by 43.9%  
603 compared to prior emissions), indicating that the existing retrieval error in HCHO  
604 measurements likely exerts an influence on the estimation of NMVOC emissions,  
605 especially in heavily polluted regions. The results highlight the significance of a  
606 thorough data validation for the HCHO column product. However, the emissions  
607 increase in the EMS2 experiment has slightly deteriorated the performance of  $\text{O}_3$   
608 simulations in the CEP2.

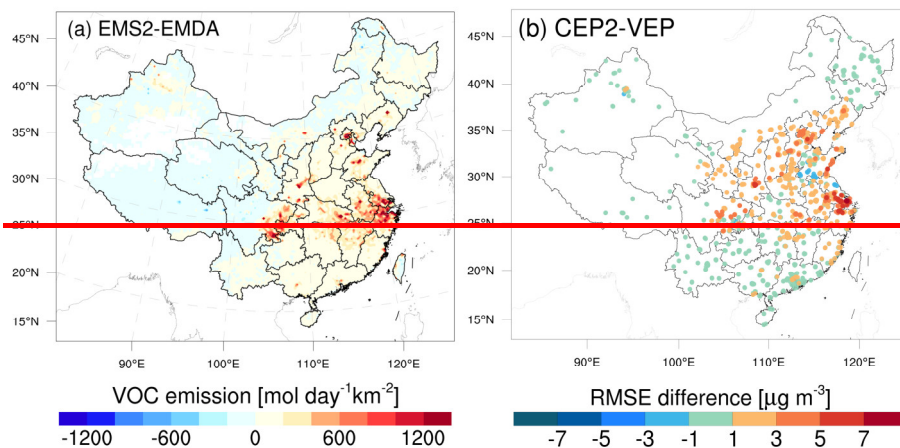
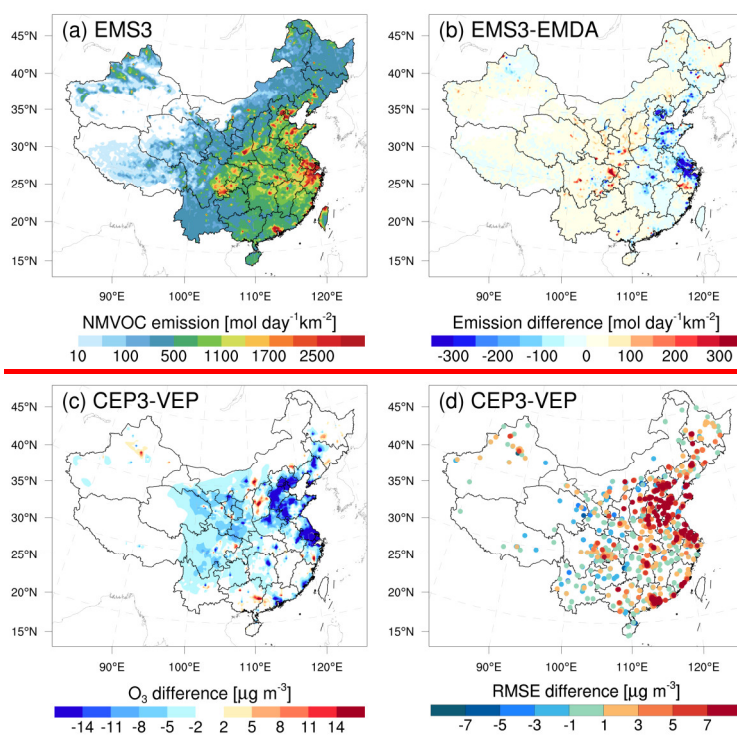


**Figure 8.** Spatial distribution of (a) differences in posterior emissions between EMS2 and EMDA, and differences in (b) RMSE between CEP2 and VEP experiments. Compared with EMDA, EMS2 reduced the TROPOMI HCHO measurements by 25% ( $< 2.5 \times 10^{15}$  molec  $\text{cm}^{-2}$ ) in clean regions and increased them by 30% ( $> 8 \times 10^{15}$  molec  $\text{cm}^{-2}$ ) in polluted regions.

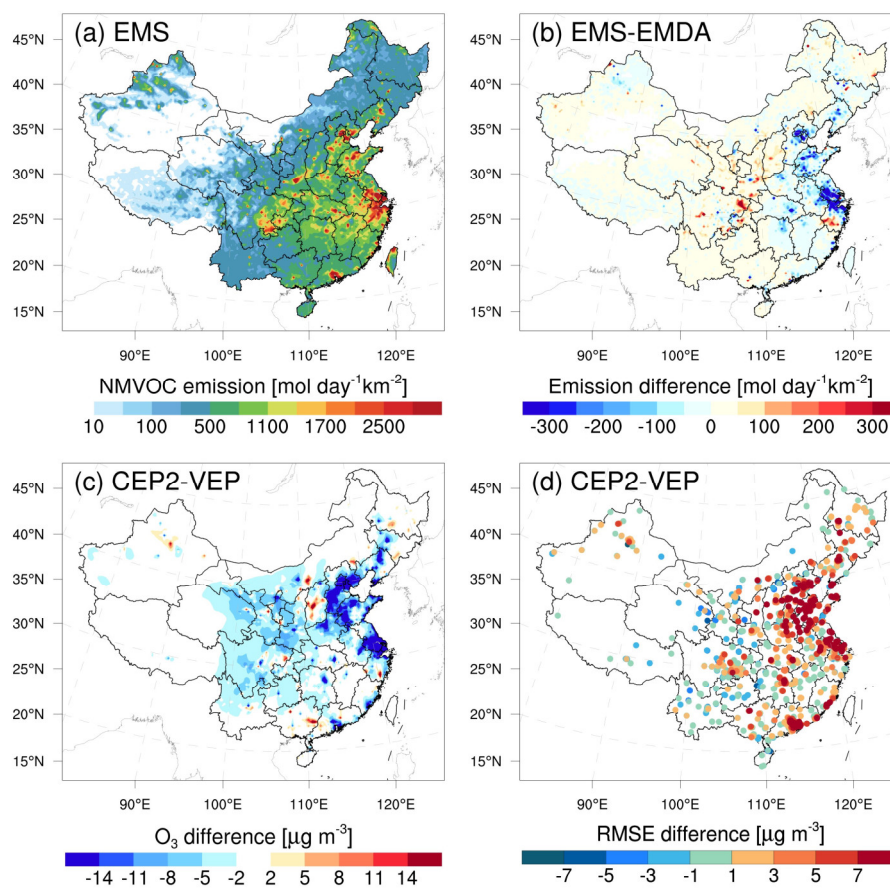
O<sub>3</sub> concentration and NO<sub>x</sub> (VOC) emissions are positively correlated in the NO<sub>x</sub> (VOC)-limited region and negatively correlated in the VOC (NO<sub>x</sub>)-limited region (Tang et al., 2011). Therefore, the uncertainty in NO<sub>x</sub> emissions can affect the model's diagnosis of O<sub>3</sub>-NO<sub>x</sub>-VOC sensitivity, thereby introducing substantial model errors in the HCHO yield from VOC oxidation. In the base inversion experiment (EMDA), we simultaneously assimilated NO<sub>2</sub> and HCHO observations to optimize NO<sub>x</sub> and NMVOC emissions. To evaluate the impact of optimized NO<sub>x</sub> emissions on O<sub>3</sub>-VOC chemistry, EMS3 disregarded the uncertainty of NO<sub>x</sub> and focused on optimizing NMVOC emissions. Compared to the EMDA, in areas where NO<sub>x</sub> is significantly overestimated, NMVOC emissions in the EMS3 have correspondingly decreased (Figure 8b). This might be due to under high-NO<sub>x</sub> conditions, HCHO production occurs promptly, thereby compensating for the substantial amount of HCHO already present in the atmosphere by reducing emissions (Chan Miller et al., 2017). Figure S108 shows comparisons of concentrations and RMSE between the simulations using posterior emissions from EMS3 and EMDA experiments. Compared to VEP, CEP3-CEP2 showed a larger RMSE, highlighting the necessity for simultaneous optimization of NO<sub>x</sub> emissions when evaluating the impact of NMVOC emission optimization on O<sub>3</sub>. Additionally, CEP2 using prior NO<sub>x</sub> emissions exhibited lower O<sub>3</sub> levels over parts of NCP and YRD, as well as some urban areas (Figure 8c), but with larger biases and

634 RMSEs (Figure 8d). The reduction in NMVOC emissions contributed to a partial  
635 decrease in O<sub>3</sub> concentration. More significantly, these areas typically align with VOC-  
636 limited mechanisms (Wang et al., 2019; Wang et al., 2021c). Therefore, the  
637 overestimation of NO<sub>x</sub> emissions (Figure S34) excessively inhibits O<sub>3</sub> accumulation  
638 due to the titration effect, thereby disrupting the evaluation of NMVOC contributions  
639 to O<sub>3</sub>. This substantial disparity also seriously affects O<sub>3</sub> source apportionment,  
640 precursor-sensitive area delineation, and emissions reduction policy formulation.



641





642

643 **Figure 8.** Spatial distribution of (a) posterior emissions in the EMS<sub>3</sub> experiment, (b)  
 644 differences in posterior emissions between EMS<sub>3</sub> and EMDA, and differences in  
 645 simulated (c) O<sub>3</sub> concentrations and (d) RMSE between CEP<sub>23</sub> and VEP experiments.  
 646 EMS<sub>3</sub> did not optimize NO<sub>x</sub> emissions compared to EMDA.

## 647 5 Summary and Conclusions

648 In this study, we extended the RAPAS assimilation system with the EnKF assimilation  
 649 algorithm to optimize NMVOC emissions using the TROPOMI HCHO retrievals.  
 650 Taking the MEIC 2020 for anthropogenic emissions and MEGANv2.1 output for  
 651 biogenic sources as a priori, NMVOC emissions over China in August 2022 were  
 652 inferred. Importantly, we implicitly took the chemical feedback among VOC-NO<sub>x</sub>-O<sub>3</sub>  
 653 into account by simultaneously adjusting NO<sub>x</sub> emissions using nationwide in-situ NO<sub>2</sub>  
 654 observations. Furthermore, we quantified the impact of NMVOC emission inversion on  
 655 surface O<sub>3</sub> pollution using the CMAQ-IRR model.

656 The application of TROPOMI HCHO observations as constraints led to a substantial  
 657 reduction of 50.2% compared to the prior emissions for NMVOCs. A domain-wide

658 significant decrease was found over central and southern China with abundant forests,  
659 especially for the broadleaf evergreen forests, implying a considerable overestimation  
660 of biogenic NMVOC emissions. Observation-constrained emissions significantly  
661 improved the performance of surface NO<sub>2</sub> and HCHO column simulations, reducing  
662 biases by 97.4% and 75.7%, respectively. This highlights the effectiveness of the  
663 RAPAS in reducing uncertainty in NO<sub>x</sub> and NMVOC emissions. Isolating the impact  
664 of NO<sub>x</sub> emission changes, the posterior NMVOC emissions significantly mitigated the  
665 overestimation in prior O<sub>3</sub> simulations, resulting in a 49.3% decrease in surface O<sub>3</sub>  
666 biases. This is mainly attributed to a substantial decrease in the RO<sub>2</sub> + NO reaction rate  
667 (a major pathway for O<sub>3</sub> production) and an increase NO<sub>2</sub> + OH reaction rate (a major  
668 pathway for O<sub>3</sub> loss) during the afternoon, resulting in a decrease in the simulated  
669 MDA8 surface O<sub>3</sub> concentrations by approximately 15 μg m<sup>-3</sup>.

670 Sensitivity inversions demonstrate the robustness of top-down emissions to variations  
671 in prior uncertainty settings, yet they are sensitive to HCHO column biases,  
672 highlighting the importance of comprehensive validation studies utilizing available  
673 remote-sensing data and, if possible, airborne validation campaigns. Moreover, we  
674 found that, in comparison to optimizing NMVOC emissions alone, the joint  
675 optimization of NMVOC and NO<sub>x</sub> emissions can significantly improve the overall  
676 performance of O<sub>3</sub> simulations. Ignoring errors in NO<sub>x</sub> emissions introduces uncertainty  
677 in quantifying the impact of NMVOC emissions on surface O<sub>3</sub>, especially in areas  
678 where overestimated NO<sub>x</sub> emissions can unrealistically amplify titration effects,  
679 highlighting the necessity of simultaneous optimization of NO<sub>x</sub> emissions.

680

### 681 **Data availability**

682 The observations used for assimilation and the optimized emissions in this study can be  
683 accessed at <https://doi.org/10.5281/zenodo.10079006> (Feng and Jiang, 2023).

684

### 685 **Author contribution**

686 SF and FJ conceived and designed the research. SF developed the data assimilation  
687 code, analyzed data, and prepared the paper with contributions from all co-authors. FJ  
688 supervised and assisted in conceptualization and writing. TQ, NW, MJ, SZ, JC, FY, and  
689 WJ reviewed and commented on the paper.

690 **Competing interests**

691 The authors declare that they have no conflict of interest.

692

693 **Acknowledgements**

694 This work is supported by the National Key R&D Program of China (Grant No.  
695 2022YFB3904801), the National Natural Science Foundation of China (Grant No:  
696 42305116 and 42377102), the Natural Science Foundation of Jiangsu Province of China  
697 (Grant No: BK20230801), and the Hangzhou Agricultural and Social Development  
698 Scientific Research Project (Grant No: 202203B29). The authors also gratefully  
699 acknowledge the High-Performance Computing Center (HPCC) of Nanjing University  
700 for doing the numerical calculations in this paper on its blade cluster system.

701

702 **References**

703 Angot, H., McErlean, K., Hu, L., Millet, D. B., Hueber, J., Cui, K., Moss, J., Wielgasz, C., Milligan,  
704 T., Ketcherside, D., Bret-Harte, M. S., and Helmig, D.: Biogenic volatile organic compound  
705 ambient mixing ratios and emission rates in the Alaskan Arctic tundra, *Biogeosciences*, 17,  
706 6219-6236, 10.5194/bg-17-6219-2020, 2020.

707 Bauwens, M., Stavrou, T., Müller, J. F., De Smedt, I., Van Roozendaal, M., van der Werf, G. R.,  
708 Wiedinmyer, C., Kaiser, J. W., Sindelarova, K., and Guenther, A.: Nine years of global  
709 hydrocarbon emissions based on source inversion of OMI formaldehyde observations, *Atmos.*  
710 *Chem. Phys.*, 16, 10133-10158, 10.5194/acp-16-10133-2016, 2016.

711 Byun, D., and Schere, K. L.: Review of the governing equations, computational algorithms, and  
712 other components of the models-3 Community Multiscale Air Quality (CMAQ) modeling  
713 system, *Applied Mechanics Reviews*, 59, 51-77, 10.1115/1.2128636, 2006.

714 Cao, H., Fu, T. M., Zhang, L., Henze, D. K., Miller, C. C., Lerot, C., Abad, G. G., De Smedt, I.,  
715 Zhang, Q., van Roozendaal, M., Hendrick, F., Chance, K., Li, J., Zheng, J., and Zhao, Y.:  
716 Adjoint inversion of Chinese non-methane volatile organic compound emissions using space-  
717 based observations of formaldehyde and glyoxal, *Atmos. Chem. Phys.*, 18, 15017-15046,  
718 10.5194/acp-18-15017-2018, 2018.

719 Chaliyakunnel, S., Millet, D. B., and Chen, X.: Constraining Emissions of Volatile Organic  
720 Compounds Over the Indian Subcontinent Using Space-Based Formaldehyde Measurements,  
721 *Journal of Geophysical Research: Atmospheres*, 124, 10525-10545, 10.1029/2019JD031262,  
722 2019.

723 Chan Miller, C., Jacob, D. J., Marais, E. A., Yu, K., Travis, K. R., Kim, P. S., Fisher, J. A., Zhu, L.,  
724 Wolfe, G. M., Hanisco, T. F., Keutsch, F. N., Kaiser, J., Min, K. E., Brown, S. S., Washenfelder,  
725 R. A., González Abad, G., and Chance, K.: Glyoxal yield from isoprene oxidation and relation  
726 to formaldehyde: chemical mechanism, constraints from SENEX aircraft observations, and  
727 interpretation of OMI satellite data, *Atmos. Chem. Phys.*, 17, 8725-8738, 10.5194/acp-17-



728 8725-2017, 2017.

729 Cheng, S., Cheng, X., Ma, J., Xu, X., Zhang, W., Lv, J., Bai, G., Chen, B., Ma, S., Ziegler, S., Donner,  
730 S., and Wagner, T.: Mobile MAX-DOAS observations of tropospheric NO<sub>2</sub> and HCHO during  
731 summer over the Three Rivers' Source region in China, *Atmos. Chem. Phys.*, 23, 3655-3677,  
732 10.5194/acp-23-3655-2023, 2023.

733 Curci, G., Palmer, P. I., Kurosu, T. P., Chance, K., and Visconti, G.: Estimating European volatile  
734 organic compound emissions using satellite observations of formaldehyde from the Ozone  
735 Monitoring Instrument, *Atmos. Chem. Phys.*, 10, 11501-11517, 10.5194/acp-10-11501-2010,  
736 2010.

737 De Smedt, I., Theys, N., Yu, H., Danckaert, T., Lerot, C., Compennolle, S., Van Roozendaal, M.,  
738 Richter, A., Hilboll, A., Peters, E., Pedergnana, M., Loyola, D., Beirle, S., Wagner, T., Eskes,  
739 H., van Geffen, J., Boersma, K. F., and Veefkind, P.: Algorithm theoretical baseline for  
740 formaldehyde retrievals from S5P TROPOMI and from the QA4ECV project, *Atmos. Meas.  
741 Tech.*, 11, 2395-2426, 10.5194/amt-11-2395-2018, 2018.

742 Elbern, H., Strunk, A., Schmidt, H., and Talagrand, O.: Emission rate and chemical state estimation  
743 by 4-dimensional variational inversion, *Atmospheric Chemistry and Physics*, 7, 3749-3769,  
744 10.5194/acp-7-3749-2007, 2007.

745 Fang, X., Shao, M., Stohl, A., Zhang, Q., Zheng, J., Guo, H., Wang, C., Wang, M., Ou, J., Thompson,  
746 R. L., and Prinn, R. G.: Top-down estimates of benzene and toluene emissions in the Pearl  
747 River Delta and Hong Kong, China, *Atmos. Chem. Phys.*, 16, 3369-3382, 10.5194/acp-16-  
748 3369-2016, 2016.

749 Feng, S., Jiang, F., Jiang, Z., Wang, H., Cai, Z., and Zhang, L.: Impact of 3DVAR assimilation of  
750 surface PM<sub>2.5</sub> observations on PM<sub>2.5</sub> forecasts over China during wintertime, *Atmospheric  
751 Environment*, 187, 34-49, 10.1016/j.atmosenv.2018.05.049, 2018.

752 Feng, S., Jiang, F., Wang, H., Wang, H., Ju, W., Shen, Y., Zheng, Y., Wu, Z., and Ding, A.: NO<sub>x</sub>  
753 Emission Changes Over China During the COVID-19 Epidemic Inferred From Surface NO<sub>2</sub>  
754 Observations, *Geophysical Research Letters*, 47, 10.1029/2020gl090080, 2020.

755 Feng, S., Jiang, F., Wang, H., Shen, Y., Zheng, Y., Zhang, L., Lou, C., and Ju, W.: Anthropogenic  
756 emissions estimated using surface observations and their impacts on PM<sub>2.5</sub> source  
757 apportionment over the Yangtze River Delta, China, *Science of The Total Environment*, 828,  
758 154522, 10.1016/j.scitotenv.2022.154522, 2022.

759 Feng, S., Jiang, F., Wu, Z., Wang, H., He, W., Shen, Y., Zhang, L., Zheng, Y., Lou, C., Jiang, Z., and  
760 Ju, W.: A Regional multi-Air Pollutant Assimilation System (RAPAS v1.0) for emission  
761 estimates: system development and application, *Geosci. Model Dev.*, 16, 5949-5977,  
762 10.5194/gmd-16-5949-2023, 2023.

763 Gaspari, G., and Cohn, S. E.: Construction of correlation functions in two and three dimensions,  
764 *Quarterly Journal of the Royal Meteorological Society*, 125, 723-757, 10.1256/smsqj.55416,  
765 1999.

766 Guenther, A. B., Jiang, X., Heald, C. L., Sakulyanontvittaya, T., Duhl, T., Emmons, L. K., and Wang,  
767 X.: The Model of Emissions of Gases and Aerosols from Nature version 2.1 (MEGAN2.1): an  
768 extended and updated framework for modeling biogenic emissions, *Geoscientific Model  
769 Development*, 5, 1471-1492, 10.5194/gmd-5-1471-2012, 2012.

770 Hong, C., Zhang, Q., He, K., Guan, D., Li, M., Liu, F., and Zheng, B.: Variations of China's emission

771 estimates: response to uncertainties in energy statistics, *Atmos. Chem. Phys.*, 17, 1227-1239,  
772 10.5194/acp-17-1227-2017, 2017.

773 Hong, Q., Liu, C., Hu, Q., Zhang, Y., Xing, C., Su, W., Ji, X., and Xiao, S.: Evaluating the feasibility  
774 of formaldehyde derived from hyperspectral remote sensing as a proxy for volatile organic  
775 compounds, *Atmospheric Research*, 264, 105777, 10.1016/j.atmosres.2021.105777, 2021.

776 Houtekamer, P. L., and Zhang, F.: Review of the Ensemble Kalman Filter for Atmospheric Data  
777 Assimilation, *Monthly Weather Review*, 144, 4489-4532, 10.1175/mwr-d-15-0440.1, 2016.

778 Jiang, X., Guenther, A., Potosnak, M., Geron, C., Seco, R., Karl, T., Kim, S., Gu, L., and Pallardy,  
779 S.: Isoprene emission response to drought and the impact on global atmospheric chemistry,  
780 *Atmospheric Environment*, 183, 69-83, 10.1016/j.atmosenv.2018.01.026, 2018.

781 Kaiser, J., Jacob, D. J., Zhu, L., Travis, K. R., Fisher, J. A., González Abad, G., Zhang, L., Zhang,  
782 X., Fried, A., Crouse, J. D., St. Clair, J. M., and Wisthaler, A.: High-resolution inversion of  
783 OMI formaldehyde columns to quantify isoprene emission on ecosystem-relevant scales:  
784 application to the southeast US, *Atmos. Chem. Phys.*, 18, 5483-5497, 10.5194/acp-18-5483-  
785 2018, 2018.

786 Li, B., Ho, S. S. H., Li, X., Guo, L., Chen, A., Hu, L., Yang, Y., Chen, D., Lin, A., and Fang, X.: A  
787 comprehensive review on anthropogenic volatile organic compounds (VOCs) emission  
788 estimates in China: Comparison and outlook, *Environment International*, 156, 106710,  
789 10.1016/j.envint.2021.106710, 2021.

790 Li, J., Chen, X., Wang, Z., Du, H., Yang, W., Sun, Y., Hu, B., Li, J., Wang, W., Wang, T., Fu, P., and  
791 Huang, H.: Radiative and heterogeneous chemical effects of aerosols on ozone and inorganic  
792 aerosols over East Asia, *Science of The Total Environment*, 622-623, 1327-1342,  
793 10.1016/j.scitotenv.2017.12.041, 2018.

794 Li, J., Nagashima, T., Kong, L., Ge, B., Yamaji, K., Fu, J. S., Wang, X., Fan, Q., Itahashi, S., Lee,  
795 H. J., Kim, C. H., Lin, C. Y., Zhang, M., Tao, Z., Kajino, M., Liao, H., Li, M., Woo, J. H.,  
796 Kurokawa, J., Wang, Z., Wu, Q., Akimoto, H., Carmichael, G. R., and Wang, Z.: Model  
797 evaluation and intercomparison of surface-level ozone and relevant species in East Asia in the  
798 context of MICS-Asia Phase III – Part 1: Overview, *Atmos. Chem. Phys.*, 19, 12993-13015,  
799 10.5194/acp-19-12993-2019, 2019.

800 Li, K., Jacob, D. J., Shen, L., Lu, X., De Smedt, I., and Liao, H.: Increases in surface ozone pollution  
801 in China from 2013 to 2019: anthropogenic and meteorological influences, *Atmos. Chem.*  
802 *Phys.*, 20, 11423-11433, 10.5194/acp-20-11423-2020, 2020.

803 Li, M., Liu, H., Geng, G., Hong, C., Liu, F., Song, Y., Tong, D., Zheng, B., Cui, H., Man, H., Zhang,  
804 Q., and He, K.: Anthropogenic emission inventories in China: a review, *National Science*  
805 *Review*, 4, 834-866, 10.1093/nsr/nwx150, 2017a.

806 Li, M., Zhang, Q., Kurokawa, J.-i., Woo, J.-H., He, K., Lu, Z., Ohara, T., Song, Y., Streets, D. G.,  
807 Carmichael, G. R., Cheng, Y., Hong, C., Huo, H., Jiang, X., Kang, S., Liu, F., Su, H., and Zheng,  
808 B.: MIX: a mosaic Asian anthropogenic emission inventory under the international  
809 collaboration framework of the MICS-Asia and HTAP, *Atmospheric Chemistry And Physics*,  
810 17, 935-963, 10.5194/acp-17-935-2017, 2017b.

811 Liu, H., Liu, Z., and Lu, F.: A Systematic Comparison of Particle Filter and EnKF in Assimilating  
812 Time-Averaged Observations, *Journal of Geophysical Research-Atmospheres*, 122, 13155-  
813 13173, 10.1002/2017jd026798, 2017.

814 Liu, Z., Wang, Y., Vrekoussis, M., Richter, A., Wittrock, F., Burrows, J. P., Shao, M., Chang, C.-C.,  
815 Liu, S.-C., Wang, H., and Chen, C.: Exploring the missing source of glyoxal (CHOCHO) over  
816 China, *Geophysical Research Letters*, 39, 10.1029/2012GL051645, 2012.

817 Marais, E. A., Jacob, D. J., Guenther, A., Chance, K., Kurosu, T. P., Murphy, J. G., Reeves, C. E.,  
818 and Pye, H. O. T.: Improved model of isoprene emissions in Africa using Ozone Monitoring  
819 Instrument (OMI) satellite observations of formaldehyde: implications for oxidants and  
820 particulate matter, *Atmos. Chem. Phys.*, 14, 7693-7703, 10.5194/acp-14-7693-2014, 2014.

821 Marsh, D. R., Mills, M. J., Kinnison, D. E., Lamarque, J.-F., Calvo, N., and Polvani, L. M.: Climate  
822 Change from 1850 to 2005 Simulated in CESM1(WACCM), *Journal of Climate*, 26, 7372-  
823 7391, 10.1175/JCLI-D-12-00558.1, 2013.

824 Mo, Z., Huang, S., Yuan, B., Pei, C., Song, Q., Qi, J., Wang, M., Wang, B., Wang, C., Li, M., Zhang,  
825 Q., and Shao, M.: Deriving emission fluxes of volatile organic compounds from tower  
826 observation in the Pearl River Delta, China, *Science of The Total Environment*, 741, 139763,  
827 10.1016/j.scitotenv.2020.139763, 2020.

828 Mu, M., Randerson, J. T., van der Werf, G. R., Giglio, L., Kasibhatla, P., Morton, D., Collatz, G. J.,  
829 DeFries, R. S., Hyer, E. J., Prins, E. M., Griffith, D. W. T., Wunch, D., Toon, G. C., Sherlock,  
830 V., and Wennberg, P. O.: Daily and 3-hourly variability in global fire emissions and  
831 consequences for atmospheric model predictions of carbon monoxide, *Journal of Geophysical  
832 Research-Atmospheres*, 116, 10.1029/2011jd016245, 2011.

833 Opacka, B., Müller, J.-F., Stavrou, T., Miralles, D. G., Koppa, A., Pagán, B. R., Potosnak, M. J.,  
834 Seco, R., De Smedt, I., and Guenther, A. B.: Impact of Drought on Isoprene Fluxes Assessed  
835 Using Field Data, Satellite-Based GLEAM Soil Moisture and HCHO Observations from OMI,  
836 *Remote Sensing*, 14, 2021, 2022.

837 Palmer, P. I., Abbot, D. S., Fu, T.-M., Jacob, D. J., Chance, K., Kurosu, T. P., Guenther, A.,  
838 Wiedinmyer, C., Stanton, J. C., Pilling, M. J., Pressley, S. N., Lamb, B., and Sumner, A. L.:  
839 Quantifying the seasonal and interannual variability of North American isoprene emissions  
840 using satellite observations of the formaldehyde column, *Journal of Geophysical Research:  
841 Atmospheres*, 111, 10.1029/2005JD006689, 2006.

842 Paulson, S. E., and Orlando, J. J.: The reactions of ozone with alkenes: An important source of HOX  
843 in the boundary layer, *Geophysical Research Letters*, 23, 3727-3730, 10.1029/96GL03477,  
844 1996.

845 Pierce, T., Geron, C., Bender, L., Dennis, R., Tonnesen, G., and Guenther, A.: Influence of increased  
846 isoprene emissions on regional ozone modeling, *Journal of Geophysical Research:  
847 Atmospheres*, 103, 25611-25629, 10.1029/98JD01804, 1998.

848 Ren, J., Guo, F., and Xie, S.: Diagnosing ozone–NO<sub>x</sub>–VOC sensitivity and revealing causes of  
849 ozone increases in China based on 2013–2021 satellite retrievals, *Atmos. Chem. Phys.*, 22,  
850 15035-15047, 10.5194/acp-22-15035-2022, 2022.

851 Seco, R., Holst, T., Davie-Martin, C. L., Simin, T., Guenther, A., Pirk, N., Rinne, J., and Rinnan, R.:  
852 Strong isoprene emission response to temperature in tundra vegetation, *Proceedings of the  
853 National Academy of Sciences*, 119, e2118014119, doi:10.1073/pnas.2118014119, 2022.

854 Skamarock, W. C., and Klemp, J. B.: A time-split nonhydrostatic atmospheric model for weather  
855 research and forecasting applications, *Journal Of Computational Physics*, 227, 3465-3485,  
856 10.1016/j.jcp.2007.01.037, 2008.

857 Souri, A. H., Nowlan, C. R., González Abad, G., Zhu, L., Blake, D. R., Fried, A., Weinheimer, A. J.,  
858 Wisthaler, A., Woo, J. H., Zhang, Q., Chan Miller, C. E., Liu, X., and Chance, K.: An inversion  
859 of NO<sub>x</sub> and non-methane volatile organic compound (NMVOC) emissions using satellite  
860 observations during the KORUS-AQ campaign and implications for surface ozone over East  
861 Asia, *Atmos. Chem. Phys.*, 20, 9837-9854, 10.5194/acp-20-9837-2020, 2020.

862 Souri, A. H., Chance, K., Bak, J., Nowlan, C. R., González Abad, G., Jung, Y., Wong, D. C., Mao,  
863 J., and Liu, X.: Unraveling pathways of elevated ozone induced by the 2020 lockdown in  
864 Europe by an observationally constrained regional model using TROPOMI, *Atmos. Chem.*  
865 *Phys.*, 21, 18227-18245, 10.5194/acp-21-18227-2021, 2021.

866 Su, W., Liu, C., Chan, K. L., Hu, Q., Liu, H., Ji, X., Zhu, Y., Liu, T., Zhang, C., Chen, Y., and Liu,  
867 J.: An improved TROPOMI tropospheric HCHO retrieval over China, *Atmos. Meas. Tech.*, 13,  
868 6271-6292, 10.5194/amt-13-6271-2020, 2020.

869 Tang, X., Zhu, J., Wang, Z. F., and Gbaguidi, A.: Improvement of ozone forecast over Beijing based  
870 on ensemble Kalman filter with simultaneous adjustment of initial conditions and emissions,  
871 *Atmospheric Chemistry And Physics*, 11, 12901-12916, 10.5194/acp-11-12901-2011, 2011.

872 van der Werf, G. R., Randerson, J. T., Giglio, L., van Leeuwen, T. T., Chen, Y., Rogers, B. M., Mu,  
873 M., van Marle, M. J. E., Morton, D. C., Collatz, G. J., Yokelson, R. J., and Kasibhatla, P. S.:  
874 Global fire emissions estimates during 1997-2016, *Earth System Science Data*, 9, 697-720,  
875 10.5194/essd-9-697-2017, 2017.

876 Vigouroux, C., Langerock, B., Bauer Aquino, C. A., Blumenstock, T., Cheng, Z., De Mazière, M.,  
877 De Smedt, I., Grutter, M., Hannigan, J. W., Jones, N., Kivi, R., Loyola, D., Lutsch, E., Mahieu,  
878 E., Makarova, M., Metzger, J. M., Morino, I., Murata, I., Nagahama, T., Notholt, J., Ortega, I.,  
879 Palm, M., Pinardi, G., Röhling, A., Smale, D., Stremme, W., Strong, K., Sussmann, R., Té, Y.,  
880 van Roozendaal, M., Wang, P., and Winkler, H.: TROPOMI–Sentinel-5 Precursor  
881 formaldehyde validation using an extensive network of ground-based Fourier-transform  
882 infrared stations, *Atmos. Meas. Tech.*, 13, 3751-3767, 10.5194/amt-13-3751-2020, 2020.

883 Wang, H., Lu, X., Seco, R., Stavroukou, T., Karl, T., Jiang, X., Gu, L., and Guenther, A. B.: Modeling  
884 Isoprene Emission Response to Drought and Heatwaves Within MEGAN Using  
885 Evapotranspiration Data and by Coupling With the Community Land Model, *Journal of*  
886 *Advances in Modeling Earth Systems*, 14, e2022MS003174, 10.1029/2022MS003174, 2022.

887 Wang, H., Yan, R., Xu, T., Wang, Y., Wang, Q., Zhang, T., An, J., Huang, C., Gao, Y., Gao, Y., Li,  
888 X., Yu, C., Jing, S., Qiao, L., Lou, S., Tao, S., and Li, Y.: Observation Constrained Aromatic  
889 Emissions in Shanghai, China, *Journal of Geophysical Research: Atmospheres*, 125,  
890 e2019JD031815, 10.1029/2019JD031815, 2020.

891 Wang, H., Wu, Q., Guenther, A. B., Yang, X., Wang, L., Xiao, T., Li, J., Feng, J., Xu, Q., and Cheng,  
892 H.: A long-term estimation of biogenic volatile organic compound (BVOC) emission in China  
893 from 2001–2016: the roles of land cover change and climate variability, *Atmos. Chem. Phys.*,  
894 21, 4825-4848, 10.5194/acp-21-4825-2021, 2021a.

895 Wang, J., Yan, R., Wu, G., Liu, Y., Wang, M., Zeng, N., Jiang, F., Wang, H., He, W., Wu, M., Ju, W.,  
896 and Chen, J. M.: Unprecedented decline in photosynthesis caused by summer 2022 record-  
897 breaking compound drought-heatwave over Yangtze River Basin, *Science Bulletin*, 68, 2160-  
898 2163, 10.1016/j.scib.2023.08.011, 2023.

899 Wang, N., Lyu, X., Deng, X., Huang, X., Jiang, F., and Ding, A.: Aggravating O<sub>3</sub> pollution due to  
900 NO<sub>x</sub> emission control in eastern China, *Science of The Total Environment*, 677, 732-744,

901 10.1016/j.scitotenv.2019.04.388, 2019.

902 Wang, P., Liu, Y., Dai, J., Fu, X., Wang, X., Guenther, A., and Wang, T.: Isoprene Emissions  
903 Response to Drought and the Impacts on Ozone and SOA in China, *Journal of Geophysical*  
904 *Research: Atmospheres*, 126, e2020JD033263, 10.1029/2020JD033263, 2021b.

905 Wang, W., van der A, R., Ding, J., van Weele, M., and Cheng, T.: Spatial and temporal changes of  
906 the ozone sensitivity in China based on satellite and ground-based observations, *Atmos. Chem.*  
907 *Phys.*, 21, 7253-7269, 10.5194/acp-21-7253-2021, 2021c.

908 Warneke, C., de Gouw, J. A., Del Negro, L., Brioude, J., McKeen, S., Stark, H., Kuster, W. C.,  
909 Goldan, P. D., Trainer, M., Fehsenfeld, F. C., Wiedinmyer, C., Guenther, A. B., Hansel, A.,  
910 Wisthaler, A., Atlas, E., Holloway, J. S., Ryerson, T. B., Peischl, J., Huey, L. G., and Hanks, A.  
911 T. C.: Biogenic emission measurement and inventories determination of biogenic emissions in  
912 the eastern United States and Texas and comparison with biogenic emission inventories,  
913 *Journal of Geophysical Research: Atmospheres*, 115, 10.1029/2009JD012445, 2010.

914 Whitaker, J. S., and Hamill, T. M.: Ensemble data assimilation without perturbed observations,  
915 *Monthly Weather Review*, 130, 1913-1924, 10.1175/1520-  
916 0493(2002)130<1913:Edawpo>2.0.Co;2, 2002.

917 Wolfe, G. M., Kaiser, J., Hanisco, T. F., Keutsch, F. N., de Gouw, J. A., Gilman, J. B., Graus, M.,  
918 Hatch, C. D., Holloway, J., Horowitz, L. W., Lee, B. H., Lerner, B. M., Lopez-Hilifiker, F.,  
919 Mao, J., Marvin, M. R., Peischl, J., Pollack, I. B., Roberts, J. M., Ryerson, T. B., Thornton, J.  
920 A., Veres, P. R., and Warneke, C.: Formaldehyde production from isoprene oxidation  
921 across NO<sub>x</sub> regimes, *Atmos. Chem. Phys.*, 16, 2597-2610, 10.5194/acp-16-2597-2016, 2016.

922 Yuan, B., Kaser, L., Karl, T., Graus, M., Peischl, J., Campos, T. L., Shertz, S., Apel, E. C., Hornbrook,  
923 R. S., Hills, A., Gilman, J. B., Lerner, B. M., Warneke, C., Flocke, F. M., Ryerson, T. B.,  
924 Guenther, A. B., and de Gouw, J. A.: Airborne flux measurements of methane and volatile  
925 organic compounds over the Haynesville and Marcellus shale gas production regions, *Journal*  
926 *of Geophysical Research: Atmospheres*, 120, 6271-6289, 10.1002/2015JD023242, 2015.

927 Zhang, M., Zhao, C., Yang, Y., Du, Q., Shen, Y., Lin, S., Gu, D., Su, W., and Liu, C.: Modeling  
928 sensitivities of BVOCs to different versions of MEGAN emission schemes in WRF-Chem  
929 (v3.6) and its impacts over eastern China, *Geosci. Model Dev.*, 14, 6155-6175, 10.5194/gmd-  
930 14-6155-2021, 2021.

931 Zhang, Q., Streets, D. G., Carmichael, G. R., He, K. B., Huo, H., Kannari, A., Klimont, Z., Park, I.  
932 S., Reddy, S., Fu, J. S., Chen, D., Duan, L., Lei, Y., Wang, L. T., and Yao, Z. L.: Asian emissions  
933 in 2006 for the NASA INTEX-B mission, *Atmos. Chem. Phys.*, 9, 5131-5153, 10.5194/acp-9-  
934 5131-2009, 2009.

935 Zheng, B., Tong, D., Li, M., Liu, F., Hong, C., Geng, G., Li, H., Li, X., Peng, L., Qi, J., Yan, L.,  
936 Zhang, Y., Zhao, H., Zheng, Y., He, K., and Zhang, Q.: Trends in China's anthropogenic  
937 emissions since 2010 as the consequence of clean air actions, *Atmospheric Chemistry And*  
938 *Physics*, 18, 14095-14111, 10.5194/acp-18-14095-2018, 2018.

939 Zhou, B., Guo, H., Zeren, Y., Wang, Y., Lyu, X., Wang, B., and Wang, H.: An Observational  
940 Constraint of VOC Emissions for Air Quality Modeling Study in the Pearl River Delta Region,  
941 *Journal of Geophysical Research: Atmospheres*, 128, e2022JD038122,  
942 10.1029/2022JD038122, 2023.

943